J. Fluid Mech. (2007), *vol.* 576, *pp.* 63–108.
doi:10.1017/S0022112006004587 Printed in the United Kingdom

Langmuir turbulence in shallow water. Part 2. Large-eddy simulation

A. E. TEJADA-MARTÍNEZ† AND C. E. GROSCH
Center for Coastal Physical Oceanography, Old Dominion University, Norfolk, VA 23509, USA

(Received 23 October 2005 and in revised form 12 October 2006)

Results of large-eddy simulation (LES) of Langmuir circulations (LC) in a wind-driven shear current in shallow water are reported. The LC are generated via the well-known Craik–Leibovich vortex force modelling the interaction between the Stokes drift, induced by surface gravity waves, and the shear current. *LC in shallow water* is defined as a flow in sufficiently shallow water that the interaction between the LC and the bottom boundary layer cannot be ignored, thus requiring resolution of the bottom boundary layer. After the introduction and a description of the governing equations, major differences in the statistical equilibrium dynamics of wind-driven shear flow and the same flow with LC (both with a bottom boundary layer) are highlighted. Three flows with LC will be discussed. In the first flow, the LC were generated by intermediate-depth waves (relative to the wavelength of the waves and the water depth). The amplitude and wavelength of these waves are representative of the conditions reported in the observations of A. E. Gargett & J. R. Wells in Part 1 (*J. Fluid Mech.* vol .000, 2007, p. 00). In the second flow, the LC were generated by shorter waves. In the third flow, the LC were generated by intermediate waves of greater amplitude than those in the first flow. The comparison between the different flows relies on visualizations and diagnostics including (i) profiles of mean velocity, (ii) profiles of resolved Reynolds stress components, (iii) autocorrelations, (iv) invariants of the resolved Reynolds stress anisotropy tensor and (v) balances of the transport equations for mean resolved turbulent kinetic energy and resolved Reynolds stresses. Additionally, dependencies of LES results on Reynolds number, subgrid-scale closure, size of the domain and grid resolution are addressed.

In the shear flow without LC, downwind (streamwise) velocity fluctuations are characterized by streaks highly elongated in the downwind direction and alternating in sign in the crosswind (spanwise) direction. Forcing this flow with the Craik–Leibovich force generating LC leads to streaks with larger characteristic crosswind length scales consistent with those recorded by observations. In the flows with LC, in the mean, positive streaks exhibit strong intensification near the bottom and near the surface leading to intensified downwind velocity 'jets' in these regions. In the flow without LC, such intensification is noticeably absent. A revealing diagnostic of the structure of the turbulence is the depth trajectory of the invariants of the resolved Reynolds stress anisotropy tensor, which for a realizable flow must lie within the Lumley triangle. The trajectory for the flow without LC reveals the typical structure of shear-dominated turbulence in which the downwind component of the resolved normal Reynolds stresses is greater than the crosswind and vertical components. In the near bottom and surface regions, the trajectory for the flow with LC driven by

† Present address: Department of Civil and Environmental Engineering, University of South Florida, Tampa, Florida, USA.

wave and wind forcing conditions representative of the field observations reveals a two-component structure in which the downwind and crosswind components are of the same order and both are much greater than the vertical component. The two-component structure of the Langmuir turbulence predicted by LES is consistent with the observations in the bottom third of the water column above the bottom boundary layer.

1. Introduction

Langmuir circulations (LC), often occurring in the wind- and wave-driven surface mixed layer of lakes and oceans, consist of pairs of parallel counter-rotating vortices (or cells) oriented approximately in the downwind direction. Originally characterized by Langmuir (1938), Langmuir cells are now generally accepted to be the result of the interaction between the wind-driven shear current and the Stokes drift current induced by surface gravity waves (Thorpe 2004). Langmuir cells are among several flow phenomena generating turbulence in the upper ocean; others include wind- or tidal-driven shear flows, buoyancy-driven convection and wave breaking. As with all turbulent flows, Langmuir turbulence encompasses a range of spatial and temporal scales. Amongst the larger spatial scales in Langmuir turbulence are those of the cells which extend in the downwind direction for tens of metres to kilometres and are separated by distances ranging from metres to as much as a kilometre (Thorpe 2004). As might be expected, a cell is neither steady nor uniformly spaced, but rather interacts with itself and other cells. In general, Langmuir turbulence is an important process for vertical mixing over a wide range of scales as well as for transport when combined with a horizontal shear current.

Thorpe (2004) reviewed the numerous field observations of LC that have been made over the last few decades. These observations include those made with vertical profilers, vector measuring current meters, backscatter intensity sonar, side-scan sonar and Doppler sonar. Most of these observations have recorded LC in the ocean surface mixed layer over deep water. As reported in Gargett & Wells (2007, hereinafter referred to as Part 1), recent field observations have led to the discovery of LC extending throughout most of the water column at a particular location on the shallow shelf coastal region of southern New Jersey undergoing strong wind and wave forcing. Such LC, reaching to the bottom boundary layer, have been termed *supercells* (Gargett *et al.* 2004; Part 1) because of their profound influence on sediment resuspension and transport. For example, on shallow shelves, currents and Langmuir supercells (LSC) driven by offshore winds can transport sediment and bioactive material episodically to the deep sea. Alternatively, episodic strong onshore winds can generate currents and LSC thereby creating favourable conditions for the transport of nutrients and biological material to shallow inner shelves (Gargett *et al.* 2004).

A model for the generation of LC was first proposed by Craik & Leibovich (1976). It consists of a vortex force (the Craik–Leibovich force or C-L force) in the momentum equations modelling the interaction between the Stokes drift, driven by the surface waves, and the vertical shear of the current; specifically, it is the vector cross-product between the Stokes drift velocity and the flow vorticity. The derivation of the Craik–Leibovich force is subtle, requiring low-pass time filtering or wave-phase averaging in order to filter out the high-frequency surface waves. Note that the averaging is not ensemble averaging so that the resulting equations are not of the RANS

(Reynolds-averaged Navier–Stokes) type. However, because of the low-pass time filtering, these equations cannot represent the complete range of space and time scales of a turbulent flow, and thus would not be appropriate for carrying out direct numerical simulations (DNS) of flows with LC. Instead, these equations can only represent a range of scales from the largest eddies to those just above the filter cutoff, and thus can be thought of as the large-eddy equations. Hereinafter, the time filtered Navier–Stokes equations with the Craik–Leibovich force will be referred to as the C-L equations.

Since the C-L equations were derived there have been a number of generalizations, extensions and applications of them. Leibovich (1977*a*) derived the C-L equations while including a wind drift current and Leibovich & Radhakrishnan (1997*b*) carried out numerical simulations of the resulting flow field for a model problem. Also, Leibovich (1977*c*) extended the equations to permit density stratification and showed that the C-L force led to a convective instability even in the presence of statically stable stratification. Craik (1977) showed that the C-L force can lead to an instability and that the Stokes drift can be that due to a random wave field. Leibovich (1983) summarized the state of knowledge of LC, both experimental and theoretical, to that date.

In the mid 1980s, work on LC continued to be focused on extensions and varied applications of the C-L equations. For example, Leibovich (1985) and Leibovich, Lele & Moroz (1989) examined nonlinear instabilities. Further work was directed toward three-dimensional LC flow as Cox & Leibovich (1993, 1994, 1997) developed 'reduced' sets of the governing equations in two spatial dimensions which reflected the flow structure in the third dimension while decoupling the upper ocean mixed layer from pycnocline motion. Leibovich & Tandon (1993) examined the three-dimensional instability of motion due to LC in water of finite depth using simplifying assumptions such as linear dependence on depth of mean shear flow, temperature and Stokes drift velocity as well as constant eddy viscosity. Later work (Tandon & Leibovich 1995*a*) showed that the unstable modes could themselves become unstable to secondary modes. Also, Tandon & Leibovich (1995*b*) carried out numerical simulations of the nonlinear equations for the same problem (but with constant density). These studies, even with simplifications, showed that a varied set of flows with LC are possible. Chini & Leibovich (2003, 2005) examined the interaction between LC and low-mode internal waves.

There have also been a number of alternative approaches to the derivation of the C-L equations. Leibovich (1980) and Craik (1985) derived the C-L equations from the generalized Lagrangian mean (GLM) equations whose exact form was first derived by Andrews & McIntyre (1978*a*, *b*). In an elegant and enlightening paper, Holm (1996) formulated the 'ideal' (inviscid) C-L equations as a Hamiltonian system. Among other results, Holm showed that the time-averaged Kelvin's circulation theorem is satisfied by the C-L equations and noted that the correct form of the C-L equations can be derived by requiring that the time-averaged Kelvin's circulation theorem be satisfied. Holm also showed that the ideal C-L equations have the same Hamiltonian structure as the Euler equations. It appears, from these results, and that of Craik (1977), that the wave field can be treated within the same conceptual framework as a turbulent flow, i.e. as a mean flow (the Stokes drift) and a fluctuating component (the random wave field).

In the last decade, substantial insight into LC has been gained from large-eddy simulations (LES). LES performed up to date have focused on the surface mixed layer over deep water, far from the bottom boundary layer. Early simulations involving the C-L equations included those of Skyllingstad & Denbo (1995), McWilliams, Sullivan &

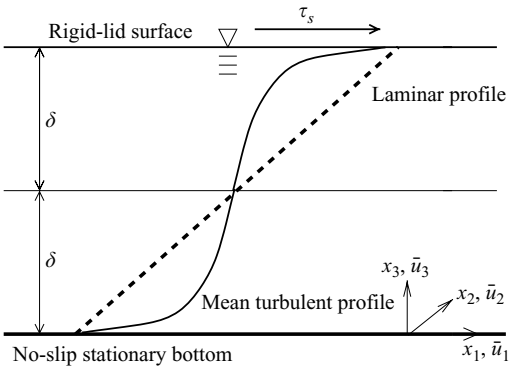

FIGURE 1. Sketch of shear flow driven by surface stress, τ_s, due to wind. The total depth is H and $\delta = H/2$. ——, mean velocity profile in a turbulent flow; – – –, linear velocity profile in a laminar flow.

Moeng (1997) and Skyllingstad *et al.* (1999). In brief, these studies found that under typical oceanic conditions LC lead to (i) homogenized mean velocity and momentum flux profiles, (ii) enhanced turbulent vertical velocity fluctuations and (iii) increased dissipation and entrainment buoyancy flux. Additionally, (iv) wave forcing (creating LC) dominated near surface turbulence, (v) dissipation rates were in good agreement with observations, (vi) the coherent downwind structures were more randomly distributed than those of prior simplified models and (vii) LC played a bigger role than convection in generating mixing. Noh, Min & Raasch (2004) and Sullivan, McWilliams & Melville (2005) added a stochastic surface force to the C-L equations in order to account for the effects of wave breaking. The latter group (in contrast to the former) found that wave breaking combined with LC can be highly effective in mixing and entrainment in the surface layer of the upper ocean. Finally, Li, Garrett & Skyllingstad (2005) performed a large number (of order 100) of simulations of shear flow in deep water and found differences in the turbulence structure between convection-dominated, shear-dominated and Langmuir-dominated turbulence. They found that mixed-layer turbulence driven by wind stress is much less important than Langmuir turbulence in typical oceanic flow except in very fetch-limited wave fields.

The observations of LSC in Gargett *et al.* 2004 and Part 1 were made under flow conditions very different from those of previous observations. In the observations in Part 1, the wavelength of the most dominant wave was approximately six times greater than the depth, corresponding to intermediate-depth waves (hereinafter *intermediate waves*) and leading to strong interaction of LC with the bottom boundary layer. In order to understand the equilibrium dynamics of LSC generated by intermediate waves, an LES approximating the environmental conditions (such as wind stress and wave field) observed by Gargett *et al.* (2004) and in Part 1 was carried out. In this LES, the flow was sufficiently resolved, especially near the bottom and top boundaries, to account directly for most of the interaction of LC with the bottom and surface boundary layers. Only a direct numerical simulation (DNS) would be able to account for all of the interaction. However, as previously noted, the C-L equations are the result of time filtering and it is clear that a DNS with these equations would not be resolving down to the Kolmogorov scales. The spatially low-pass-filtered C-L equations were solved numerically inside a horizontally periodic domain in which the flow was driven by a constant wind stress at the top surface and was made to satisfy a no-slip boundary condition at the bottom wall (plate) (figure 1); no-normal

flow was enforced at the top surface. Numerous simulations were performed varying the forcing conditions in order to determine the sensitivity of the results to these conditions. These studies showed the similarities (and differences) between Langmuir turbulence and Couette-flow turbulence.

The previously described flow configuration without C-L forcing is a type of Couette flow. Traditionally, turbulent Couette flow is simulated via two parallel no-slip plates moving in opposite directions. Somewhat surprisingly, Couette turbulence (for which the governing equations do not have the C-L force), exhibits some of the characteristics of Langmuir turbulence. Lee & Kim (1991) performed numerous simulations of turbulent Couette flow and showed the existence of streaks of high (positive) and low (negative) streamwise velocity fluctuations on horizontal (cross-stream/streamwise) planes. These large-scale streaks possess much greater length scales than the classical *wall streaks* observed on near-wall horizontal planes of turbulent Poiseuille flow. Visualization of the flow on cross-stream/vertical planes, i.e. normal to the streamwise direction, showed the large-scale streaks appearing as 'vortical' cell patterns extending almost from top to bottom. Other numerical and laboratory studies of turbulent Couette flow were those of Bech *et al.* (1995) and Papavassiliou & Hanratty (1997). Bech *et al.* (1995) were able to verify the cross-stream alternating high-speed/low-speed pattern of the Couette streaks. Through direct numerical simulation, Papavassiliou & Hanratty (1997) provided insight into the dynamics governing the cells and streaks. They found that the large-scale Couette cells can receive energy from the small scale turbulence, contrary to the common energy cascade notion in which the large scales always pass energy to the small scales. They showed that far from the boundaries, in the core region, the Couette structures are nearly inviscid and are not greatly affected by turbulent stresses or viscous diffusion. Papavassiliou & Hanratty demonstrated that when the flow reaches statistical equilibrium (i.e. stationarity) the mean streamwise vorticity (characterizing the strength of the Couette cells) is nearly constant along mean flow streamlines. Tsukahara & Kawamura (2004) demonstrated that the Couette streaks are not an artefact of the limited dimensions (lengths) of the computational domain, as they were able to show the existence of the cells over a wide range of dimensions. Furthermore, they showed that in low-Reynolds-number turbulent Couette flows, the characteristic cross-stream length scale of the Couette streaks does not depend on the Reynolds number, but rather on the height of the domain.

The general features of turbulent Couette flow, i.e. the streaks and cells, are similar to those of wind-driven turbulent shear flow with LC in the presence of bottom and surface boundary layers. However, the equilibrium dynamics of turbulent Couette flow are very different from those of the flow with LC. An extremely important diagnostic showing the difference is the map of the invariants of the resolved Reynolds stress anisotropy tensor (Lumley 1978; Pope 2000) as a function of distance from the bottom. Hereinafter, the large-scale streaks in Couette turbulence are referred to as *Couette streaks* in order to distinguish them from *wall streaks* and *Langmuir streaks*, and the corresponding large-scale cells are referred to as *Couette cells* in order to distinguish them from *Langmuir supercells*.

The structure of the rest of the paper is as follows. After a brief description of the governing equations, the major differences in the equilibrium dynamics between wind-driven turbulent shear flow in the presence of bottom and surface boundary layers (i.e. wind-driven turbulent Couette flow) and the same flow with LC generated by the Craik–Leibovich force under conditions representative of the observations in Part 1 are highlighted. (Statistical equilibrium is described in Appendix C, immediately following

equation (C 7).) This comparison will rely on flow visualizations and diagnostics including mean velocity profiles, autocorrelations, invariants of the resolved Reynolds stress anisotropy tensor and balances of the transport equations for the resolved mean turbulent kinetic energy and the resolved Reynolds stress tensor. Remarks will be made along the way comparing simulation results with the observations. The LC in the observations in Part 1 were generated by intermediate waves. In addition to investigating this case numerically, a case in which the LC were generated by shorter waves as well as a third case in which the LC were generated by waves of greater amplitude, are investigated. Finally, conclusions and suggestions for additional studies will be given. The Appendixes will address effects of Reynolds number, domain size, grid cell size and subgrid-scale closure. The Appendixes also include details of the numerical method.

2. Governing equations

Constant-density flow is assumed because the LSC described in Part 1 were observed in approximately neutrally stable water. The flow of interest (figure 1) is driven by a constant surface stress. Periodicity is imposed in the horizontal (x_1 and x_2) directions and a no-slip boundary condition is imposed at the bottom. Zero normal flow is imposed at the surface. Periodicity in x_1 and x_2 implies that the flow is spatially homogeneous over these directions. The governing equations and numerical method (see Appendix E) will be described within the context of this flow configuration.

2.1. *The spatially filtered Craik–Leibovich equations*

Application of a homogeneous low-pass spatial filter to the non-dimensionalized C-L equations leads to

$$\frac{\partial \bar{u}_i}{\partial x_i} = 0, \tag{2.1a}$$

$$\frac{\partial \bar{u}_i}{\partial t} + \bar{u}_j \frac{\partial \bar{u}_i}{\partial x_j} = -\frac{\partial \bar{\Pi}}{\partial x_i} + \frac{1}{Re}\frac{\partial^2 \bar{u}_i}{\partial x_j^2} + \frac{\partial \tau_{ij}}{\partial x_j} + \frac{1}{La_t^2}\epsilon_{ijk}\phi_j^s \bar{\omega}_k, \tag{2.1b}$$

where ϵ_{ijk} is the totally antisymmetric third-rank tensor, an overbar denotes application of the low-pass spatial filter and $\bar{u}_i$ and $\bar{\omega}_i$ are the ith components of the non-dimensional space- and time-filtered velocity and vorticity, respectively, in the Cartesian coordinate system (x_1, x_2, x_3) depicted in figure 1. Recall that the C-L equations govern the behaviour of time-filtered variables. Furthermore, the C-L equations were spatially filtered, leading to the equations (2.1); hence, $\bar{u}_i$ and $\bar{\omega}_i$ are referred to as the *space- and time-filtered* velocity and vorticity, respectively. The non-dimensional, modified, space- and time-filtered pressure is defined as

$$\bar{\Pi} = \bar{p} + \tfrac{1}{2}\Gamma, \tag{2.2}$$

where $\bar{p}$ is the non-dimensional, space- and time-filtered pressure and

$$\Gamma = \frac{1}{La_t^4}\phi_i^s\phi_i^s + \frac{2}{La_t^2}\bar{u}_i\phi_i^s. \tag{2.3}$$

The fourth (last) term on the right-hand side of (2.1b) is the non-dimensionalized C-L vortex force defined as the Stokes drift velocity crossed with the filtered vorticity. The non-dimensional Stokes drift velocity is defined by Phillips (1967) and LeBlond &

Mysak (1978) as

$$\phi_1^s = \frac{\cosh(2\kappa x_3)}{2\sinh^2(\kappa H)}, \qquad \phi_2^s = \phi_3^s = 0, \tag{2.4}$$

where H is the water depth and κ is the dominant wavenumber of the filtered-out surface gravity waves.

The characteristic flow velocity is taken as the friction velocity, u_τ, where $u_\tau = (\tau_s/\rho_o)^{1/2}$, τ_s is the constant wind stress in the x_1-direction applied at the top surface (as depicted in figure 1) and ρ_o is the constant density. Non-dimensionalizing the governing equations with characteristic flow velocity u_τ and characteristic length scale $\delta = H/2$ gives rise to the turbulent Langmuir number, $La_t = (u_\tau/u_s)^{1/2}$, and the Reynolds number $Re = u_\tau\delta/\nu$ (with ν the kinematic viscosity) appearing in (2.1). The characteristic Stokes drift velocity is defined as $u_s = \omega\kappa a^2$, where ω is the dominant frequency, κ is the dominant wavenumber and a is the amplitude of the surface gravity waves.

Expanding the C-L vortex force on the right-hand side of (2.1), it can be seen that it is simply the Stokes drift velocity crossed with the filtered vorticity. The components of the C-L force are $(0, -\bar{\omega}_3, \bar{\omega}_2)\phi_1^s/La_t^2$. Note that the C-L force does not contribute to the x_1-momentum equation because the Stokes drift velocity is zero in the x_2 and x_3 directions.

An important difference between the equations used in previous LES of flows with LC (such as those of McWilliams *et al.* 1997; Li *et al.* 2005; and others) and the equations (2.1) is that in the latter the viscous stress term (inversely proportional to Re) has been retained. The viscous stress term has been retained because the present simulations partially resolve bottom and surface viscous boundary layers where this term plays an important role in the governing dynamics. Previous simulations focused on flows with LC within the surface mixed layer of the deep ocean far from the bottom boundary layer, thus the viscous stress term could be neglected. Note that the current simulations partially resolve bottom and surface viscous boundary layers as they are LES and not DNS.

2.2. *Subgrid-scale closure*

The subgrid-scale (SGS) stress τ_{ij} in (2.1), generated by spatial filtering the C-L equations, is defined as

$$\tau_{ij} = \bar{u}_i\bar{u}_j - \overline{u_i u_j}. \tag{2.5}$$

The term $\overline{u_i u_j}$ gives rise to a closure problem and thus must be parameterized. The deviatoric part of τ_{ij} (i.e. $\tau_{ij}^d \equiv \tau_{ij} - \delta_{ij}\tau_{kk}/3$) is parameterized using the dynamic Smagorinsky closure and the dilatational part (i.e. $\delta_{ij}\tau_{kk}/3$) is added to the modified pressure, $\bar{\Pi}$. The Smagorinsky closure expresses the deviatoric part of the SGS stress as

$$\tau_{ij}^d = 2\underbrace{(C_s\bar{\Delta})^2|\bar{S}|}_{\text{Eddy viscosity}}\bar{S}_{ij}, \tag{2.6}$$

where $\bar{\Delta}$ is the width of the grid filter (i.e. the smallest characteristic length scale resolved by the discretization), C_s is the Smagorinsky coefficient, $\bar{S}_{ij} = (\bar{u}_{i,j} + \bar{u}_{j,i})/2$ is the filtered strain-rate tensor, and $|\bar{S}| = (2\bar{S}_{ij}\bar{S}_{ij})^{1/2}$ is its norm. The model coefficient is computed dynamically (Lilly 1992) as

$$(C_s\bar{\Delta})^2 = \frac{1}{2}\frac{\langle L_{ij}M_{ij}\rangle}{\langle M_{kl}M_{kl}\rangle}, \tag{2.7}$$

where

$$L_{ij} = \widetilde{\overline{u}_i \overline{u}_j} - \widetilde{\overline{u}}_i \widetilde{\overline{u}}_j, \tag{2.8}$$

and

$$M_{ij} = \widetilde{|\overline{S}|\overline{S}_{ij}} - \alpha^2 |\widetilde{\overline{S}}| \widetilde{\overline{S}}_{ij}. \tag{2.9}$$

An over-tilde, $\tilde{\cdot}$, denotes application of a homogeneous low-pass spatial test filter in the x_1 and x_2 directions. Angle brackets in (2.7) denote averaging in x_1 and x_2 as a means of preventing instabilities due to potential negative values of the model coefficient. Finally, α is a parameter referred to as the filter width ratio and often approximated as the test filter width divided by the grid cell size, h. All of the simulations described here were performed using the well-known box filter of width $2h$ (Pope 2000) approximated using the trapezoidal rule. The width of the resulting discrete filter is $\sqrt{6}h$ (Lund 1997), thus $\alpha = \sqrt{6}$.

In Appendix C, a different closure is considered in order to verify that results are not greatly sensitive to the subgrid-scale stress. The numerical method used to solve the previously described governing equations is given in detail in Appendix E.

3. Results

In this section, the major differences in the equilibrium dynamics between a flow with C-L vortex forcing and the corresponding flow without the C-L vortex forcing are emphasized. Where possible, the LES results with C-L vortex forcing are compared to the observations reported in Part 1.

3.1. *Shear turbulence versus Langmuir turbulence*

The following two simulations are compared: (i) shear flow driven by a surface wind stress with C-L vortex forcing and (ii) shear flow driven by the same surface wind stress without LC. Both flows were in the presence of bottom and surface boundary layers. In both cases the constant surface wind stress was applied such that $Re = 395$ based on friction velocity as described earlier. Note that in these simulations, the Reynolds number based on bulk velocity is $Re_b = 6800$. Case (i) is characterized by $La_t = 0.7$ and $\lambda = 6H$, where λ is the dominant wavelength of surface waves and H is the water depth. Note that $\kappa = 2\pi/\lambda$ in (2.4). These values for La_t and λ are representative of the coastal shelf shear flow with LSC observed in Part 1. Furthermore, $\lambda = 6H$ corresponds to intermediate waves. Case (ii) is characterized by $La_t = \infty$, thus no LC. Note that Re representative of the observations is much greater than that of the present simulation ($Re = 395$). As shown in Appendix A, a simulation of flow with LC at a lower Reynolds number ($Re = 180$) was performed without great changes in the results, demonstrating that the flow with LC reaches Reynolds-number independence at much lower values than the Reynolds numbers characteristic of the observations.

As was discussed in the previous section, earlier workers did not resolve the bottom boundary layer in their LES of flows with LC, thus the viscous stress and consequently the Reynolds number did not appear in their formulation. More specifically, the viscous stress was assumed negligible compared to the subgrid-scale stress, a reasonable assumption valid far from boundary layers. For those cases, in which molecular viscosity does not play a dominant role in the flow dynamics, an alternative Reynolds number may be computed based on the eddy or turbulent viscosity associated with the subgrid-scale stress. For example, in the LES of McWilliams *et al.* (1997) the mid-depth of the computational domain was 45 m, the friction velocity associated with the wind stress was $6.1 \times 10^{-3}\,\mathrm{m\,s^{-1}}$ and the eddy viscosity is $O(10^{-3})\,\mathrm{m^2\,s^{-1}}$.

Thus, the Reynolds number based on eddy viscosity was approximately 274.5, lower than the Reynolds number in the current simulations at $Re = 395$.

The current wind-driven shear flow without C-L forcing in the presence of bottom and surface boundary layers gives rise to the same turbulent structures found in Couette flow driven by oppositly moving parallel no-slip plates. Thus, following the direct numerical simulations of turbulent Couette flow at about $Re = 170$ of Lee & Kim (1991), the domain dimensions for both cases, (i) and (ii), were chosen as $(L_1/\delta, L_2/\delta, L_3/\delta) = (4\pi, 8\pi/3, 2)$. Here L_1, L_2 and L_3 are the lengths of the domain in the x_1-, x_2- and x_3-direction, respectively, as sketched in figure 1. Note that the spanwise length of the computational domain in both flows is $L_2 = 8\pi\delta/3 = 4.19H$ where the water depth is $H = 2\delta$. This length falls within the range of values reported for the spanwise length of one Langmuir cell ($3H$–$6H$) in Part 1; thus, it was expected that one Langmuir cell could be resolved in the flow with LC. In Appendix B, results are presented with a computational domain of greater spanwise extent. The computational grid in flows both with and without LC contained 96 points in x_1, 96 points in x_2 and 97 points in x_3 ($96 \times 96 \times 97$). The stretching parameter in the mapping function in (E 9) (in Appendix E) was set to $b = 0.973$. This value of b was chosen so that the horizontal plane of grid points closest to the bottom wall (top surface) was at a distance of 1 wall unit (i.e. $u_\tau \Delta x_3/\nu = 1$, where Δx_3 is the distance in regular units) from the bottom wall (top surface), well within the expected viscous sublayer near the bottom wall. The non-dimensional time step was chosen as 0.001 for both cases in order to yield temporal accuracy and not violate the well-known Courant, Friedrichs and Lewy condition.

3.1.1. *Visualizations*

To visualize the flow, it is convenient to represent the LES solution using the classical Reynolds decomposition. Thus,

$$\bar{u}_i = \langle \bar{u}_i \rangle + \bar{u}_i', \tag{3.1}$$

where $\langle \cdot \rangle$ denotes averaging in time and over the horizontal directions (x_1 and x_2) and $\bar{u}_i'$ is the fluctuation of the resolved velocity. The decomposition in (3.1) can also be used to compute the resolved Reynolds stresses as

$$\langle \bar{u}_i' \bar{u}_j' \rangle = \langle \bar{u}_i \bar{u}_j \rangle - \langle \bar{u}_i \rangle \langle \bar{u}_j \rangle, \tag{3.2}$$

assuming the flow is in statistical equilibrium. Profiles of resolved Reynolds stresses will be shown later.

Figure 2 shows colour maps of instantaneous downwind fluctuating velocity, $\bar{u}_1'$, on the horizontal plane at mid-depth in the flows with and without LC. In both flows there is at least one pair of high- and low-speed regions or streaks highly elongated in the downwind (streamwise) direction (x_1) and alternating in the crosswind (spanwise) direction (x_2). In the flow with no LC (figure 2*b*) there are two streaks with $\bar{u}_1' > 0$ and two with $\bar{u}_1' < 0$. The spanwise width of each streak is approximately equal to the depth, H, in agreement with the Couette streaks originally found in the simulation of Lee & Kim (1991). Animations reveal that when the C-L vortex force is turned on, the streaks where $\bar{u}_1' > 0$ merge, as the flow transitions from two pairs of streaks to one pair. Figure 2(*a*) shows the one-pair structure characterizing the flow with LC. The width of the streak with $\bar{u}_1' > 0$ is approximately $3H$ and the width of the streak with $\bar{u}_1' < 0$ is approximately H.

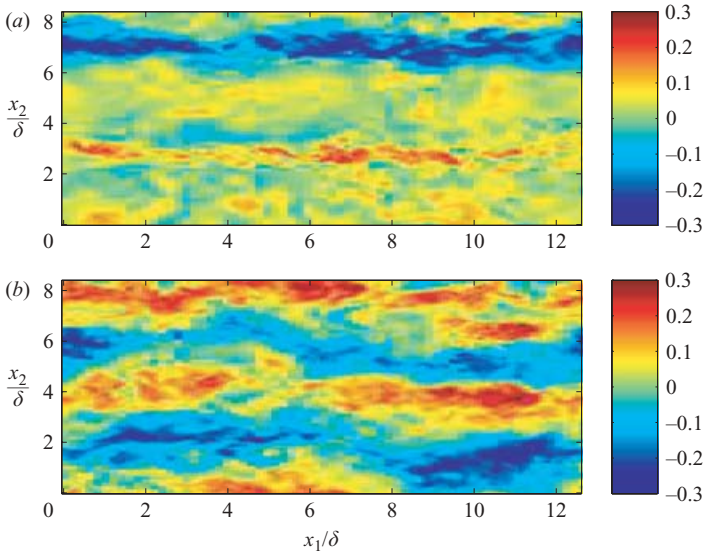

FIGURE 2. Colour maps of instantaneous $\bar{u}_1'$ on the horizontal (x_1, x_2)-plane at mid-depth $(x_3 = H/2)$ in flows (a) with (b) and without LC at $Re = 395$. In flow with LC, $La_t = 0.7$ and $\lambda = 6H$. Fluctuations $\bar{u}_1'$ are normalized by the mean centreline streamwise velocity, U_1^c.

A second decomposition of the LES solution can be taken as

$$\bar{u}_i = \langle \bar{u}_i \rangle + \underbrace{\langle \bar{u}_i' \rangle_{tx_1} + \bar{u}_i''}_{=\bar{u}_i'}, \tag{3.3}$$

where $\langle \cdot \rangle_{tx_1}$ denotes averaging in time and over the downwind (x_1) direction and $\bar{u}_i'$ is obtained from (3.1). For simplicity, let $\bar{v}_i'(x_2, x_3) = \langle \bar{u}_i' \rangle_{tx_1}$. This partially averaged fluctuation emphasizes flow structures which are coherent in the downwind direction; it provides further information about the secondary flow structures (i.e. the streaks) already observed in figure 2. Figures 3 and 4 show the crosswind/vertical structure of this term in the flows with and without LC, respectively. Overall, both flows exhibit positive and negative spanwise cell structures in each of the partially averaged fluctuating velocity components; the flow with LC has a spanwise *one-cell* structure while the flow without LC has a spanwise *two-cell* structure. As will be discussed shortly, the one-cell structure in the flow with C-L forcing possesses all of the basic characteristics of the Langmuir supercells (LSC) observed in Part 1; hence, this is, indeed, a flow containing one LSC, as expected.

In the mean as defined by $\langle \cdot \rangle_{tx_1}$, the flow with LC has much stronger maxima and minima in all fluctuating velocity components compared to the flow without LC: extrema of $\bar{v}_1'$, $\bar{v}_3'$ and $\bar{v}_2'$ are approximately 3, 2.5 and 10 times greater, respectively.

As seen in figure 3(a), the flow with LC is characterized by intensification of positive $\bar{v}_1'$ near the surface and near the bottom, consistent with the observations of LSC in Part 1. Furthermore, the region of positive $\bar{v}_1'$ exhibits a mushroom-shaped pattern. In the case of the flow without LC, there is no near-bottom or near-surface intensification as the magnitude of $\bar{v}_1'$ is nearly uniform (either positive or negative) in most of the water column.

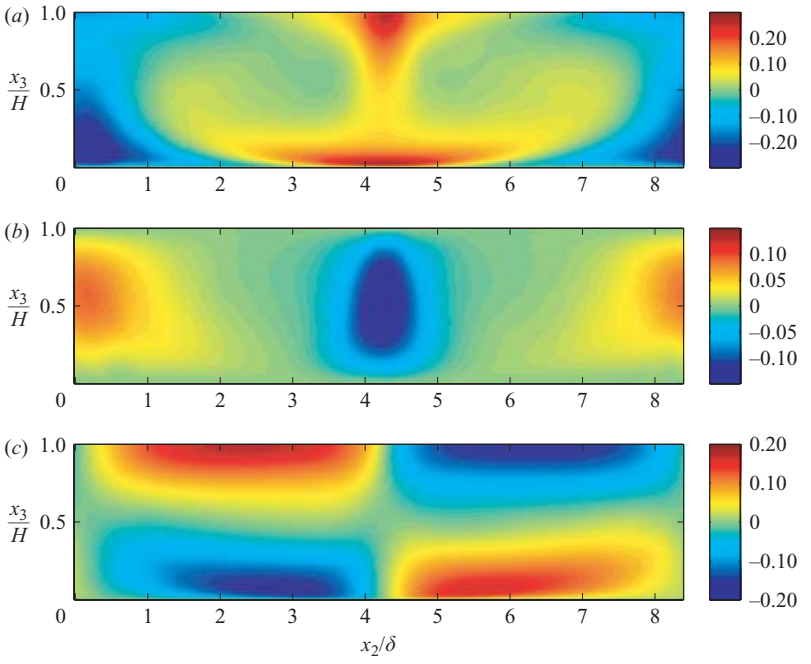

FIGURE 3. Colour maps of partially averaged fluctuating velocity components (normalized by U_1^c) on the (x_2, x_3)-plane for flow with LC at $Re = 395$ ($La_t = 0.7$, $\lambda = 6H$). (*a*) $\bar{v}_1'/U_1^c$, (*b*) $\bar{v}_3'/U_1^c$, (*c*) $\bar{v}_2'/U_1^c$.

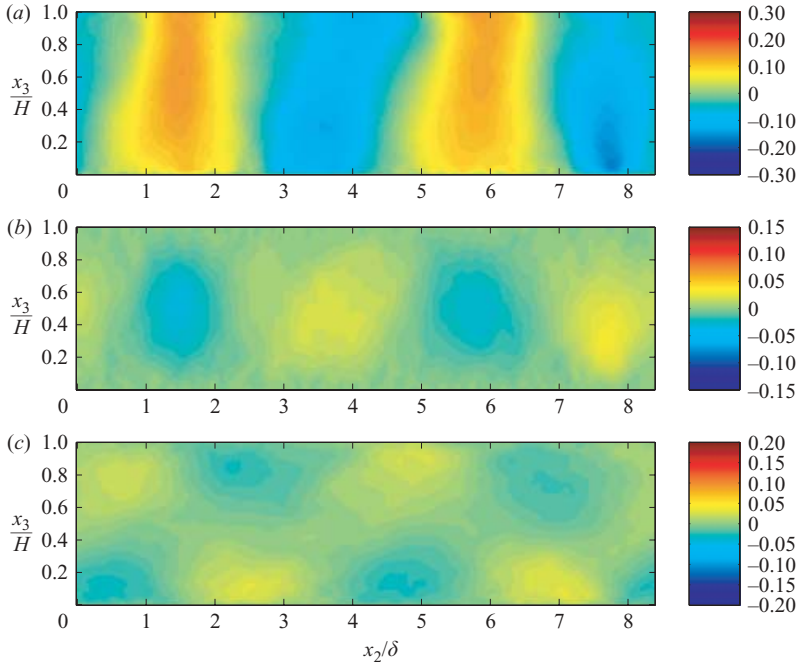

FIGURE 4. Colour maps of partially averaged fluctuating velocity components (normalized by U_1^c) on the (x_2, x_3)-plane for flow without LC at $Re = 395$. (*a*) $\bar{v}_1'/U_1^c$, (*b*) $\bar{v}_s'/U_1^c$, (*c*) $\bar{v}_2'/U_1^c$.

In both flows, a region of positive $\bar{v}_1'$ coincides with a region of negative $\bar{v}_3'$ and vice versa. Regions of positive $\bar{v}_3'$ are referred to as *upwelling limbs* and regions of negative $\bar{v}_3'$ are referred to as *downwelling limbs*. In the flow with LC, the ratio of the spanwise length of the upwelling limb to the spanwise length of the downwelling limb (r) is 1.4 at mid-depth ($x_3 = H/2$), which compares favourably with the 1.1 to 1.3 range recorded in the observations of LSC in Part 1. The value of r is greater than unity throughout most of the water column. Owing to conservation of mass, this results in an downwelling limb with greater intensity (magnitude) of $\bar{v}_3'$ than the upwelling limb. Furthermore, the extremum of $\bar{v}_3'$ in the downwelling limb occurs slightly above mid-depth, in general agreement with the observations in Part 1. In the flow without LC, r is approximately 1 throughout most of the water column, thus the magnitude of $\bar{v}_3'$ in the downwelling limbs is nearly constant through most of the water column and is nearly the same as in the upwelling limbs.

As seen in figures 3(c) and 4(c), in both flows, a region of downwelling coincides with a region of surface convergence and bottom divergence of $\bar{v}_2'$. Finally, in the flow with LC, extrema of $\bar{v}_2'$ occur at the surface (consistent with observations discussed in Part 1), in contrast to the flow without LC where extrema of $\bar{v}_2'$ occur in the upper third of the water column.

To summarize, in the mean (as defined by $\langle\cdot\rangle_{tx_1}$), the Craik–Leibovich force induces two parallel torques, one in the downwind direction and the other in the opposite direction, as sketched by Leibovich (1983). These torques generate counter-rotating vortices aligned in the wind direction, as noted by Leibovich (1983). The torques induce converging crosswind velocity fluctuations at the surface (seen in figure 3c) and thus surface convergence of the flow. Owing to conservation of mass, this convergence generates the downwelling region pictured in figure 3(b) in addition to the surface intensification of downwind fluctuations in figure 3(a). In the lower portion of the water column, again owing to conservation of mass, the downwelling region induces diverging spanwise fluctuations (and thus divergence of the flow at the bottom) as well as bottom intensification of downwind fluctuations.

3.1.2. *Autocorrelations*

Autocorrelation functions give further insight into the turbulent flow structures previously visualized. The two-point one-time streamwise correlation function is defined as

$$R_{ij}^{x}(\Delta x_1, x_3) = \frac{\langle \bar{u}_i'(t, x_1, x_2, x_3)\bar{u}_j'(t, x_1 + \Delta x_1, x_2, x_3)\rangle_{tx_2}}{\langle \bar{u}_i'\bar{u}_j'\rangle}. \tag{3.4}$$

Similarly, the spanwise correlation function is

$$R_{ij}^{y}(\Delta x_2, x_3) = \frac{\langle \bar{u}_i'(t, x_1, x_2, x_3)\bar{u}_j'(t, x_1, x_2 + \Delta x_2, x_3)\rangle_{tx_1}}{\langle \bar{u}_i'\bar{u}_j'\rangle}, \tag{3.5}$$

where $\langle\cdot\rangle_{tx_i}$ denotes averaging in time and over the x_i-direction. Autocorrelations are obtained by setting $i = j$ in (3.4) and (3.5) and ignoring the usual convention of summing over repeated indices.

Three sets of autocorrelation functions are shown in figures 5 to 7. The first demonstrates the coherency of turbulent fluctuations near the top surface at a distance of approximately 20.11 wall units ($u_\tau \Delta x_3/\nu \approx 20.11$) below the surface, the second at mid-depth and the third at approximately 20.11 wall units above the bottom (i.e. within the buffer layer of the bottom wall boundary layer). Figure 5(a) reveals the existence of streamwise structures in $\bar{u}_1'$ near the surface in the flows with and

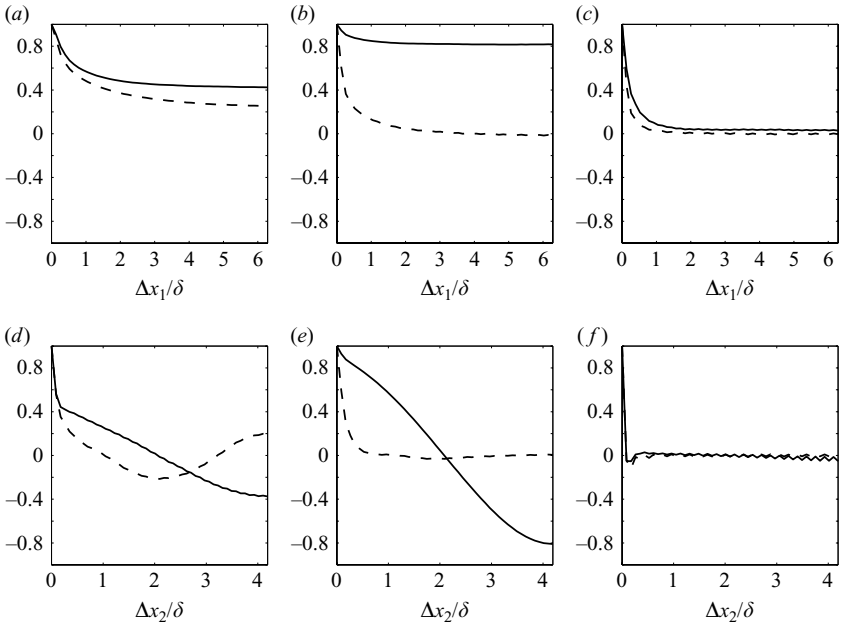

FIGURE 5. Autocorrelations near the top surface at a distance $u_\tau \Delta x_3/\nu \approx 20.11$ away from the surface in flows with and without LC; Δx_3 is the distance from the surface in units of $\delta = H/2$. In both flows, $Re = 395$ and in flow with LC, $La_t = 0.7$ and $\lambda = 6H$. ———, flow with LC; – – –, flow without LC. (*a*) R^x_{11}, (*b*) R^x_{22}, (*c*) R^x_{33}, (*d*) R^y_{11}, (*e*) R^y_{22}, (*f*) R^y_{33}.

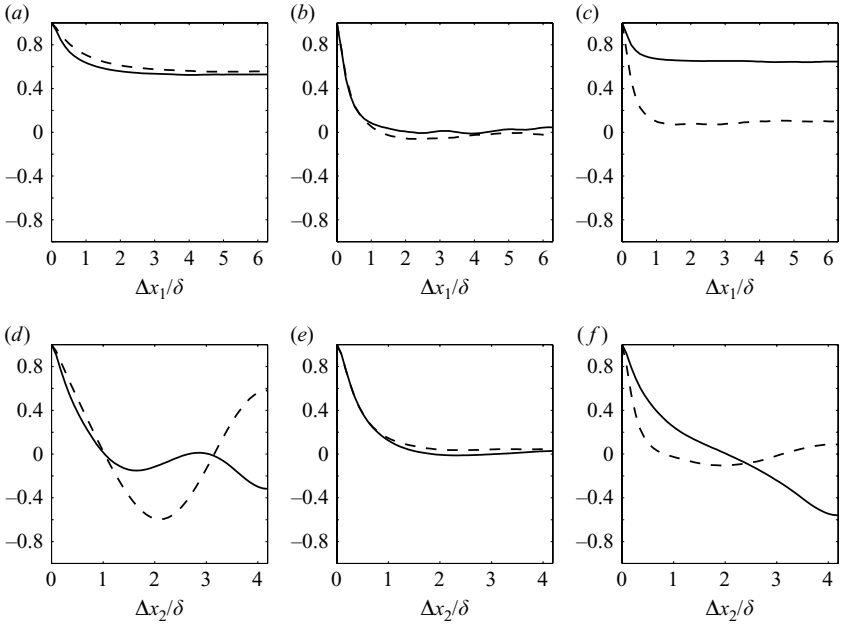

FIGURE 6. Autocorrelations at mid-depth in flows with and without LC. In both flows, $Re = 395$ and in flow with LC, $La_t = 0.7$ and $\lambda = 6H$. ———, flow with LC; – – –, flow without LC. (*a*) R^x_{11}, (*b*) R^x_{22}, (*c*) R^x_{33}, (*d*) R^y_{11}, (*e*) R^y_{22}, (*f*) R^y_{33}.

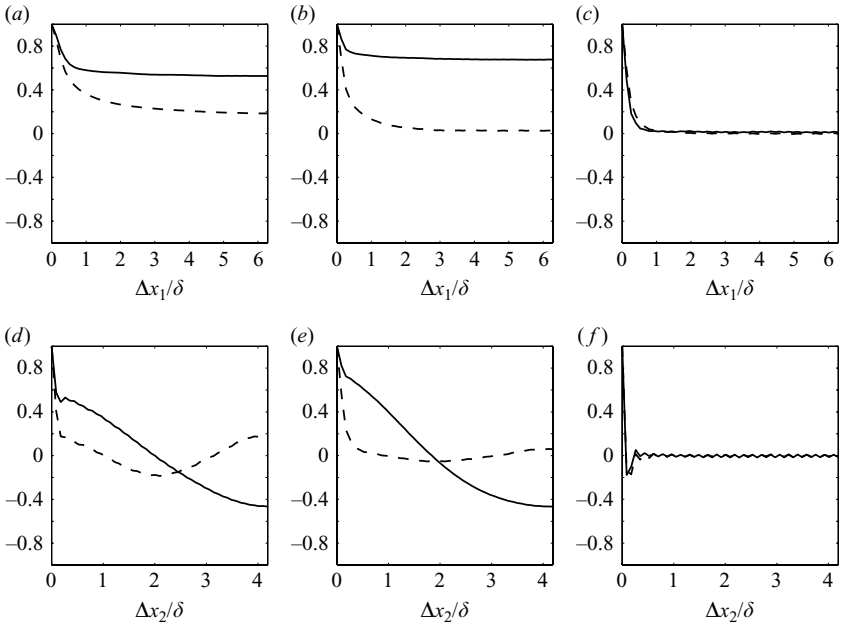

FIGURE 7. Autocorrelations near the bottom wall at a distance $u_\tau \Delta x_3/\nu \approx 20.11$ away from the wall in flows with and without LC; Δx_3 is the distance from the wall in units of $\delta = H/2$. In both flows, $Re = 395$ and in flow with LC, $La_t = 0.7$ and $\lambda = 6H$. ———, flow with LC; – – –, flow without LC. (*a*) R^x_{11}, (*b*) R^x_{22}, (*c*) R^x_{33}, (*d*) R^y_{11}, (*e*) R^y_{22}, (*f*) R^y_{33}.

without LC. In the flow with LC, the near-surface intensification of $\bar{v}'_2$ (figure 3*c*) is mirrored in the slight decrease of R^x_{22} to about less than 0.8 at large Δx_1 (figure 5*b*). In contrast, in the flow without LC, R^x_{22} decays to zero-consistent with the surface attenuation of $\bar{v}'_2$ (figure 7*c*). The spanwise autocorrelations in figure 5(*d*) reveal the single-cell and two-cell crosswind structures in $\bar{u}'_1$ characterizing the flows with and without LC, respectively, a feature shown previously in terms of $\bar{v}'_1$. For the flow with LC near the surface, figure 5(*e*) demonstrates that the single-cell structure present in $\bar{v}'_2$ is also present in $\bar{u}'_2$. This single-cell structure is highly coherent owing to the surface intensification of $\bar{u}'_2$. However, this is not case for the flow without LC, as the autocorrelation decays quickly to nearly zero, given that there is no surface intensification of $\bar{u}'_2$. As expected, there is little evidence of any structure in $\bar{u}'_3$ near the surface in both flows where $\bar{u}'_3 \approx 0$ owing to the zero normal flow boundary condition at the surface.

At mid-depth, the autocorrelations in figure 6(*a*) show the existence of the streamwise structure in $\bar{u}'_1$ for both flows, with and without LC. Furthermore, figure 6(*d*) shows the single-cell and two-cell crosswind structures in $\bar{u}'_1$ characterizing the flows. In the flow with LC, R^y_{11} exhibits two modes. The higher mode corresponds to the the mushroom-shaped pattern exhibited by the single-cell structure (figure 3*a*), while the lower mode corresponds to the single cell structure itself. In figures 6(*b*) and 6(*e*), autocorrelations R^x_{22} and R^y_{22} decay rapidly to zero for both flows because $\bar{u}'_2$ is nearly zero at mid-depth, as expected from the colour maps of $\bar{v}'_2$ in figures 3(*c*) and 4(*c*). Figures 6(*c*) and 6(*f*) show that the mid-depth downwind and crosswind structure of $\bar{u}'_3$ is more coherent in the flow with LC than in the flow without. In other words, the Couette streaks tend to meander more than the Langmuir streaks.

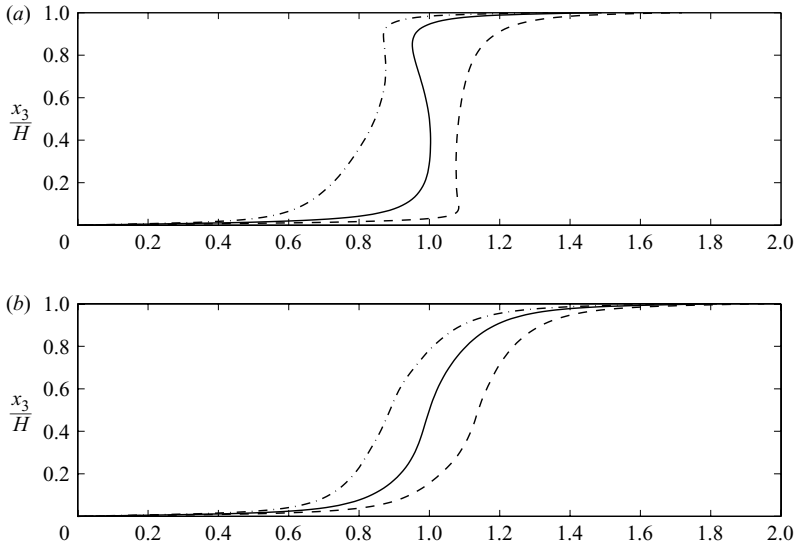

FIGURE 8. Vertical variation of mean velocity normalized by U_1^c in flows (*a*) with and (*b*) without LC at $Re = 395$. In flow with LC, $La_t = 0.7$ and $\lambda = 6H$. ———, $\langle \bar{u}_1 \rangle / U_1^c$; – – –, $\langle \bar{u}_1 \rangle_{tx_1} / U_1^c$ in a downwelling limb; — · —, $\langle \bar{u}_1 \rangle_{tx_1} / U_1^c$ in an upwelling limb.

The variation of the autocorrelations near the bottom (figure 7) is very similar to that near the surface. The existence of a near-bottom intensification in $\bar{u}_1'$ similar to that of $\bar{v}_1'$ (figure 3*a*) is evident in the relatively high values of the autocorrelation of $\bar{u}_1'$ for the flow with LC, shown in figure 7(*a*). Near-bottom intensification occurs in $\bar{u}_2'$ as well. As in the two previous figures, the single-cell crosswind structure in the flow with LC as compared to the double-cell structure in the flow without LC is evident. The coherency characterizing fluctuations at 20.11 wall units above the bottom boundary clearly suggest that the Langmuir cells extend at least into the buffer layer just above the viscous sublayer.

In summary, the autocorrelations presented here provide further evidence for the existence of and differences between Couette and Langmuir cells, both structures persisting from the near bottom to the near surface of the water column. Furthermore, results confirm the existence of Couette cells at $Re = 395$. Previously, Couette cells had been found at $Re = 170$ and lower.

3.1.3. *Mean velocity*

Figures 8 and 9 show mean streamwise velocity for the flows with and without LC. In both cases, given that the wind stress driving the flow in the x_1-direction is constant, the slope of the mean streamwise velocity $\langle \bar{u}_1 \rangle$ at the bottom wall is within numerical error (i.e. 1 %) of the value at the top surface, as expected owing to conservation of downwind momentum. This can be seen in the solid lines in figure 8 depicting $\langle \bar{u}_1 \rangle$ in both flows. Furthermore, in both flows the mean spanwise velocity $\langle \bar{u}_2 \rangle$ and the mean vertical velocity $\langle \bar{u}_3 \rangle$ (not shown) are nearly zero. A major difference between the two flows occurs in $\langle \bar{u}_1 \rangle$. In the flow with LC, the LC serve to homogenize $\langle \bar{u}_1 \rangle$ throughout most of the water column. This behaviour can be seen in figure 8(*a*) where $\langle \bar{u}_1 \rangle$ is roughly constant in the region below mid-depth, resulting in almost no vertical mean shear. In the upper portion of the water column, the slope

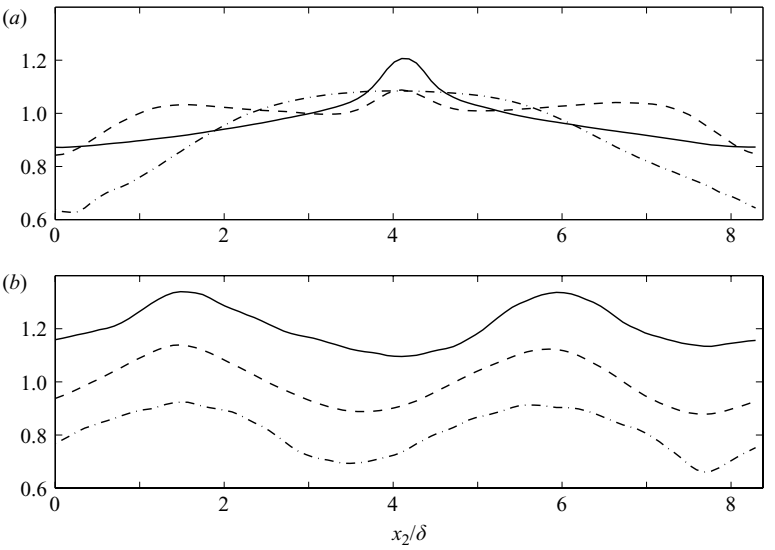

FIGURE 9. Spanwise variation of mean velocity normalized by U_1^c in flows (a) with and (b) without LC. In both flows, $Re = 395$ and in flow with LC, $La_t = 0.7$ and $\lambda = 6H$. ———, $\langle\bar{u}_1\rangle_{tx_1}/U_1^c$ at a distance $u_\tau \Delta x_3/\nu \approx 67$ away from the top surface; – – –, $\langle\bar{u}_1\rangle_{tx_1}/U_1^c$ at mid-depth; — · —, $\langle\bar{u}_1\rangle_{tx_1}/U_1^c$ at a distance $u_\tau \Delta x_3/\nu \approx 67$ away from the bottom wall.

of $\langle\bar{u}_1\rangle$ becomes slightly negative, resulting in slightly negative mean vertical shear. In the flow without LC, $\langle\bar{u}_1\rangle$ has non-zero, positive slope throughout the entire water column. The homogenizing action of the LC serves to decrease the mean streamwise bulk velocity, U_b, defined as the depth average of $\langle\bar{u}_1\rangle$. As a result, the skin friction coefficient at the bottom increases by about 20 %. The skin friction coefficient may be defined in terms of U_b and the shear bottom stress τ_w, as $C_f = 2\tau_w/\rho U_b^2$. In the flow with LC, $C_f = 0.006$, whereas in the flow without LC, $C_f = 0.005$.

Next, the effect of the downwelling and upwelling limbs on the streamwise mean velocity are explored by analysing profiles of $\langle\bar{u}_1\rangle_{tx_1}$. In the flow with LC, in the downwelling limb, the boundary layer exhibited by $\langle\bar{u}_1\rangle_{tx_1}$ is much thinner than in the upwelling limb. In the lower portion of the water column excluding the near-wall region, $\langle\bar{u}_1\rangle_{tx_1}$ in the downelling limb is better mixed than in the upwelling limb. In the upper portion of the water column excluding the near-surface region, in the downwelling limb, $\langle\bar{u}_1\rangle_{tx_1}$ possesses positive slope, whereas in the upwelling limb its slope becomes negative. Thus, the downwelling limb plays an important role in the homogenization of $\langle\bar{u}_1\rangle$, especially in the lower portion of the water column. The upwelling limb contributes mostly to the negative slope characterizing $\langle\bar{u}_1\rangle$ in the upper portion of the water column.

In the flow without LC, the effects of the downwelling and upwelling limbs on $\langle\bar{u}_1\rangle$ approximately cancel each other out throughout the entire water column (figure 8b).

Figure 9 shows the spanwise variation of $\langle\bar{u}_1\rangle_{tx_1}$ near the surface, at mid-depth and near the bottom of the water column in both flows. The near surface and near bottom intensification of positive $\bar{v}_1'$ lead to downwind velocity 'jets' with different characteristics throughout the water column, as demonstrated by $\langle\bar{u}_1\rangle_{tx_1}$ in figure 9(a). In the lower portion of the water column, the jet spreads over a wider spanwise length than in the upper portion of the water column; at mid-depth, the spread is widest. In

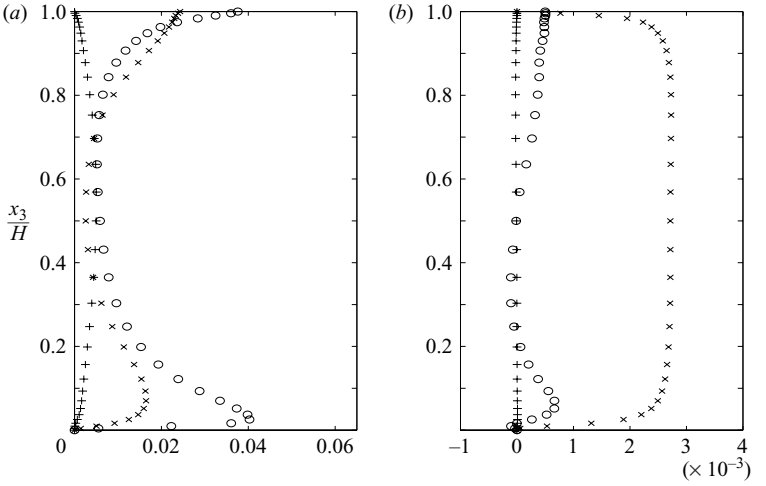

FIGURE 10. Profiles of resolved Reynolds stresses for flow with LC ($La_t = 0.7, \lambda = 6H$) at $Re = 395$. (*a*) Normal stresses. ○, $\langle \bar{u}_1' \bar{u}_1' \rangle$; ×, $\langle \bar{u}_2' \bar{u}_2' \rangle$; +, $\langle \bar{u}_3' \bar{u}_3' \rangle$. (*b*) Shear stresses. ○, $-\langle \bar{u}_1' \bar{u}_2' \rangle$; ×, $-\langle \bar{u}_1' \bar{u}_3' \rangle$; +, $-\langle \bar{u}_2' \bar{u}_3' \rangle$. Velocities and stresses are normalized by U_1^c and $U_1^{c\,2}$, respectively. For visual clarity, every third point of the discrete profiles is plotted.

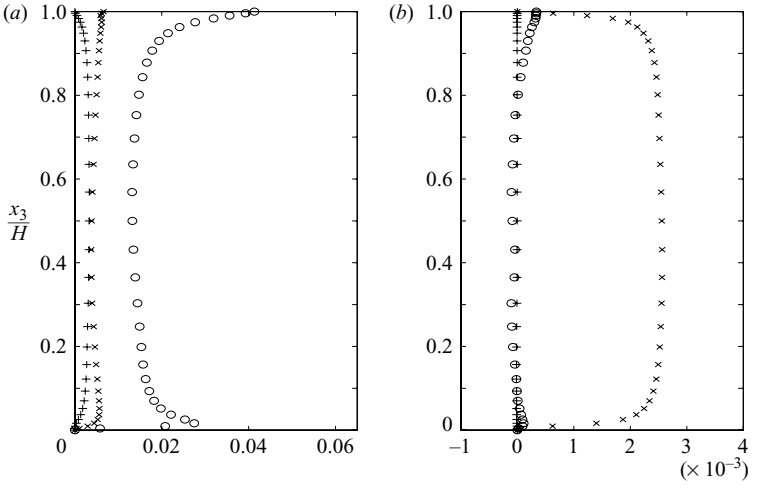

FIGURE 11. Profiles of resolved Reynolds stresses for flow without LC at $Re = 395$. (*a*) Normal stresses. (*b*) Shear stresses. Symbols as in figure 10. For visual clarity, every third point of the discrete profiles is plotted.

the flow without LC, the spread of the jets caused by regions of positive $\bar{v}_1'$ is uniform throughout most of the water column.

3.1.4. *Resolved Reynolds stresses*

Figures 10(*a*) and 11(*a*) show normalized resolved normal Reynolds stress components for the flows with and without LC, respectively. There are several distinguishing differences between the two cases. First, in the lower portion of the water column, the LC case possesses larger values of $\langle \bar{u}_1' \bar{u}_1' \rangle$ and $\langle \bar{u}_2' \bar{u}_2' \rangle$. In the no LC case, ordering of components is $\langle \bar{u}_1' \bar{u}_1' \rangle > \langle \bar{u}_2' \bar{u}_2' \rangle > \langle \bar{u}_3' \bar{u}_3' \rangle$ for the entire water column.

In the LC case, this ordering changes, as in the lower part of the water column $\langle \bar{u}_1' \bar{u}_1' \rangle > \langle \bar{u}_2' \bar{u}_2' \rangle > \langle \bar{u}_3' \bar{u}_3' \rangle$ while in the middle $\langle \bar{u}_1' \bar{u}_1' \rangle > \langle \bar{u}_3' \bar{u}_3' \rangle > \langle \bar{u}_2' \bar{u}_2' \rangle$. Towards the upper part of the water column the ordering changes to $\langle \bar{u}_2' \bar{u}_2' \rangle > \langle \bar{u}_1' \bar{u}_1' \rangle > \langle \bar{u}_3' \bar{u}_3' \rangle$ and at the surface it settles back to $\langle \bar{u}_1' \bar{u}_1' \rangle > \langle \bar{u}_2' \bar{u}_2' \rangle > \langle \bar{u}_3' \bar{u}_3' \rangle$.

Throughout most of the lower half of the water column, the flow with LC possesses larger values of $\langle \bar{u}_1' \bar{u}_1' \rangle$ than the flow without LC. The opposite occurs in the upper half of the water column. For the most part, these differences between the flows can be traced to the production of $\langle \bar{u}_1' \bar{u}_1' \rangle$ by mean shear. Although production by mean shear is proportional to the mean vertical shear as well as to $\langle \bar{u}_1' \bar{u}_3' \rangle$, the former is the dominant factor. Furthermore, although the C-L force does not directly affect the production of $\langle \bar{u}_1' \bar{u}_1' \rangle$ (as will be shown later), it affects production indirectly through homogenization of mean downwind velocity. In the flow with LC, the LC tend to homogenize the mean downwind velocity giving rise to a lower mean vertical shear throughout the upper 90 % of the water column compared to the flow without LC. Consequently, production rates of $\langle \bar{u}_1' \bar{u}_1' \rangle$ are lower in the upper half of the water column. In the lower 10 % of the water column of the flow with LC, the mean vertical shear is greater than in the flow without LC, thus leading to higher production rates near the bottom.

Differences between the two flows in $\langle \bar{u}_2' \bar{u}_2' \rangle$ and $\langle \bar{u}_3' \bar{u}_3' \rangle$ can be directly attributed to the C-L vortex force, as in the flow with LC, the C-L force directly affects the production rates of these stress components. For example, as will be shown later, near the surface, the C-L force acts as the main source of $\langle \bar{u}_2' \bar{u}_2' \rangle$, leading to higher values in the flow with LC than in the flow without LC. Near the surface in the flow without LC, pressure strain redistribution acts as the main source of $\langle \bar{u}_2' \bar{u}_2' \rangle$, but at much lower rates than the C-L force in the flow with LC.

Figures 10(*b*) and 11(*b*) show normalized resolved shear Reynolds stress components for the flow with and without LC, respectively. $\langle \bar{u}_1' \bar{u}_3' \rangle$ components for both cases are close to each other in magnitude throughout most of the water column; for the LC case, $\langle \bar{u}_1' \bar{u}_3' \rangle$ attains slightly greater values, especially near the middle of the water column. The normalized magnitude of $\langle \bar{u}_1' \bar{u}_3' \rangle$ in both cases is in agreement with that recorded in the field observations. Additionally, for both cases, $\langle \bar{u}_2' \bar{u}_3' \rangle$ is nearly zero throughout the entire water column. For the flow without LC, this also occurs with $\langle \bar{u}_1' \bar{u}_2' \rangle$. In flow with LC, the C-L vortex force induces slight variations in $\langle \bar{u}_1' \bar{u}_2' \rangle$ near the bottom and near the surface. It is important that the data recorded in the field observations exhibit a non-zero $\langle \bar{u}_1' \bar{u}_2' \rangle$ component, presumably owing to a non-zero mean velocity in x_2, $\langle u_2 \rangle$ (see Part 1). This is in contrast to the current simulations for which $\langle \bar{u}_2 \rangle$ is nearly zero.

It is of interest to examine how much the Couette and Langmuir cells contribute to the energetics. Using the Reynolds decomposition in (3.1) and assuming that the flow is stationary, the resolved turbulent kinetic energy is expressed as

$$\bar{q} \equiv \tfrac{1}{2} \langle \bar{u}_i' \bar{u}_i' \rangle = \tfrac{1}{2} (\langle \bar{u}_i \bar{u}_i \rangle - \langle \bar{u}_i \rangle \langle \bar{u}_i \rangle). \tag{3.6}$$

Furthermore, the resolved turbulent kinetic energy may be re-expressed in terms of the decomposition in (3.3) as

$$\bar{q} = \tfrac{1}{2} (\langle \bar{u}_i'' \bar{u}_i'' \rangle + \langle \bar{v}_i' \bar{v}_i' \rangle) + \langle \bar{v}_i' \bar{u}_i'' \rangle. \tag{3.7}$$

As seen through the visualizations shown earlier, $\bar{v}_i'$ is the part of the resolved velocity fluctuations associated with Langmuir and Couette cells. Figure 12 sheds light on how important the Langmuir and Couette cells are on the resolved turbulent kinetic energy. Here, it can be seen that the contribution to turbulent kinetic energy (TKE) from the Langmuir cells (i.e. $\langle \bar{v}_i' \bar{v}_i' \rangle / 2$) in the flow with LC is much greater than the contribution

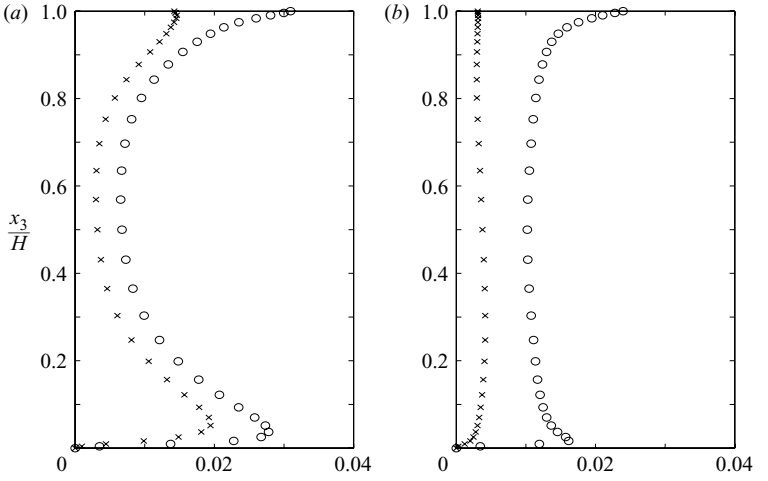

FIGURE 12. Profiles of resolved turbulent kinetic energy (TKE) and its contribution from secondary flow associated with (*a*) Langmuir cells in flow with LC and (*b*) Couette cells in flow without LC. Both flows are at $Re = 395$. In flow with LC, $La_t = 0.7$ and $\lambda = 6H$. ○, resolved TKE ($\bar{q}$); ×, contribution to resolved TKE from fluctuations associated with Langmuir cells in (*a*) and Couette cells in (*b*) ($\langle \bar{v}_i' \bar{v}_i' \rangle / 2$).

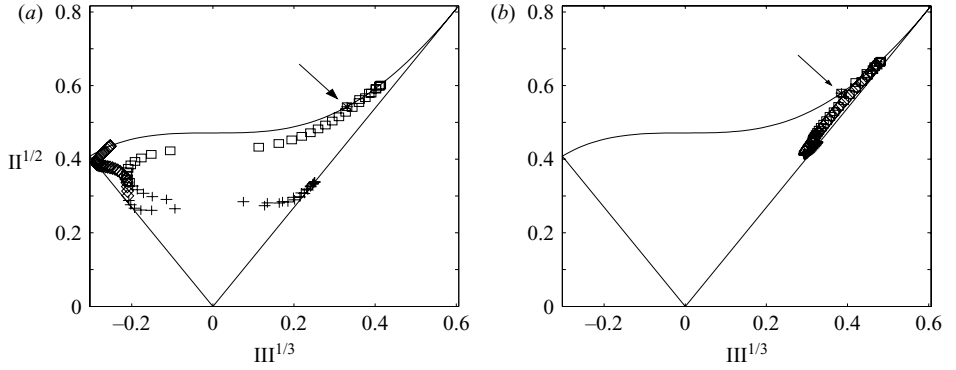

FIGURE 13. Lumley triangle for flows (*a*) with and (*b*) without LC at $Re = 395$. In flow with LC, $La_t = 0.7$ and $\lambda = 6H$. □, $x_3/H \in (0, 1/3]$; +, $x_3/H \in (1/3, 2/3]$; ◇, $x_3/H \in (2/3, 1]$. The solid indicated by the arrow denotes the map at the first point off the bottom wall.

to TKE from the Couette cells in the flow without LC. Throughout the upper half of the water column, the total resolved TKE is about the same for both cases. However, in the lower portion of the water column, the resolved TKE in the flow with LC peaks at a value about twice as large as that in the flow without LC. In addition, the portion of the resolved TKE due to the cells is only 15 % to 40 % of the total for the flow without LC whereas it is 50 % to 80 % of the total for the flow with LC.

Figure 13 shows maps of the Lumley invariants (Pope 2000) for the flows with and without LC. The Lumley invariant map is helpful in understanding the state of anisotropy of the resolved Reynolds stresses. The map is built from the second and third invariants of the anisotropy tensor $b_{ij} = \langle u_i' u_j' \rangle / 2\bar{q} - \delta_{ij}/3$, where the resolved turbulent kinetic energy, $\bar{q}$, is defined in (3.6). The second and third invariants are $\mathrm{II} = b_{ij} b_{ji}$ and $\mathrm{III} = b_{ij} b_{jk} b_{ki}$; the first invariant is $\mathrm{I} = \mathrm{trace}\{b_{ij}\} = 0$. In figure 13, the

quantity $II^{1/2}$ serves as a measure of the magnitude of the anisotropy, while the location of the coordinate ($II^{1/2}$, $III^{1/3}$) serves as a measure of the shape of the anisotropy and thus the state of the resolved turbulence. All realizable states of fluctuating motion are constrained to lie within the triangular region shown in the figure. The linear sides of the Lumley triangle emanating from the origin represent axisymmetric turbulence; the origin represents three-dimensional isotropic turbulence. The region of the triangle in which $III > 0$ represents turbulence for which the Reynolds stress ellipsoid (see Pope 2000) is a prolate spheroid with two-eigenvalues of the Reynolds stress tensor smaller than the third, hereinafter referred to as the cigar-shaped state. The region in which $III < 0$ represents turbulence for which the Reynolds stress ellipsoid is an oblate spheroid with two eigenvalues larger than the third, hereinafter referred to as the pancake-shaped state. The upper left-hand side vertex of the triangle corresponds to two-component isotropic turbulence, while the upper right-hand side vertex corresponds to one-component turbulence.

Figure 13 shows the trajectories of the Lumley invariant maps varying from $x_3/H = 0$ (bottom wall) to $x_3/H = 1$ (top surface) for the flows with and without LC. For both flows, the fluctuating motion is two-component (near the right-hand side of the top bounding curve of the Lumley triangle) very close to the bottom wall because $\langle \bar{u}'_3 \bar{u}'_3 \rangle$ is much smaller than the other two normal Reynolds stress components. In the case of the flow without LC, the fluctuating motion moves close to a cigar-shaped axisymmetric state (near the right-hand-side edge of the triangle) as the distance away from the bottom wall increases. The reason for this behaviour is that $\langle \bar{u}'_1 \bar{u}'_1 \rangle$ is larger than $\langle \bar{u}'_2 \bar{u}'_2 \rangle \approx \langle \bar{u}'_3 \bar{u}'_3 \rangle$, especially in the middle region of the water column. In the upper-half region of the water column, the fluctuating motion moves back towards the two-component state (near the right-hand side of the top bounding curve of the triangle).

The trajectory of the invariant map exhibited by the flow with no LC is characteristic of shear-dominated turbulence. LC tends to decrease mean shear thus a different behaviour is expected for the flow with LC. For the case with LC, as distance from the wall increases, the turbulence moves towards a pancake-shape (two-component) state as the trajectory of the map goes into the interior of the triangle towards the left-hand-side edge. The reason for this behaviour is that $\langle \bar{u}'_1 \bar{u}'_1 \rangle$ and $\langle \bar{u}'_2 \bar{u}'_2 \rangle$ are much greater than $\langle \bar{u}'_3 \bar{u}'_3 \rangle$ throughout most of the bottom third portion of the water column. This is no longer true in the region $0.35 < x_3/H < 0.45$ as the ordering $\langle \bar{u}'_1 \bar{u}'_1 \rangle > \langle \bar{u}'_3 \bar{u}'_3 \rangle \approx \langle \bar{u}'_2 \bar{u}'_2 \rangle$ holds and the turbulence shifts back to an axisymmetric cigar-shaped state. In the upper-half of the water column, as distance to the top surface decreases, the turbulence moves back to the pancake-shaped state. At the surface, the turbulence assumes an approximately two-component isotropic state (the upper left-hand-side vertex of the triangle) because $\langle \bar{u}'_1 \bar{u}'_1 \rangle \approx \langle \bar{u}'_2 \bar{u}'_2 \rangle$ and $\langle \bar{u}'_3 \bar{u}'_3 \rangle = 0$. The trajectory of the Lumley invariant map in the bottom third of the water column for the flow with LC (figure 13*a*) closely resembles the shape of the map based on data from the field observations in Part 1. Furthermore, it highlights the vast difference in turbulent motion between the flows with and without LC.

3.2. *Balances of budgets of resolved turbulent kinetic energy and Reynolds stresses*

Next, balances of resolved mean turbulent kinetic energy (TKE) and resolved Reynolds stress budgets in the previously discussed flows with and without LC at $Re = 395$ are studied under statistical equilibrium. Transport equations for TKE and Reynolds stresses are given in Appendix D. Under statistical equilibrium, the terms on the right-hand side of each of these equations sum to zero. In addition to

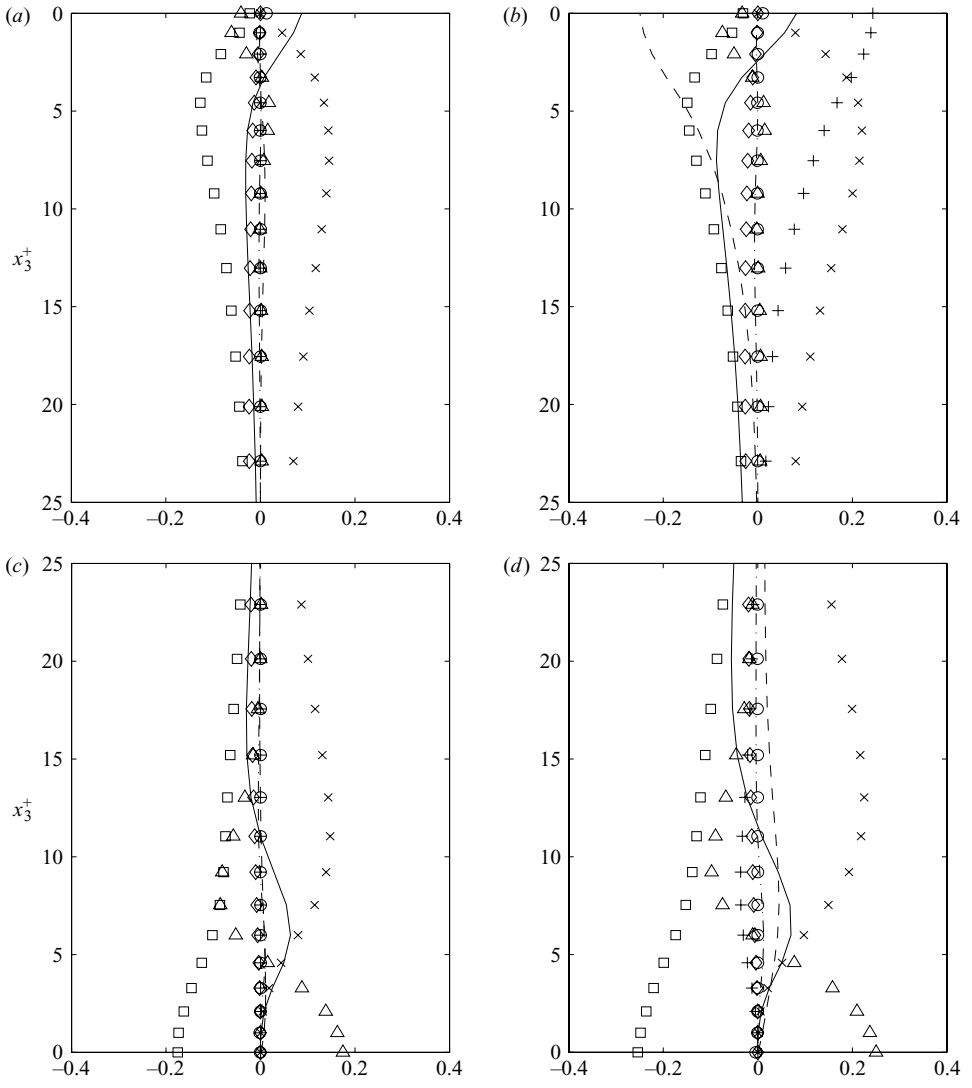

FIGURE 14. (a, b) Near-top surface and (c, d) near-bottom wall budgets of resolved turbulent kinetic energy in flows with and without LC (i.e. LC flow and no LC flow) at $Re = 395$. In flow with LC, $\lambda = 6H$ and $La_t = 0.7$. Terms are normalized by viscous scales (Pope 2000) and distances are expressed in wall units. In (a) and (b), location of top surface is at $x_3^+ = 0$. In (c) and (d), location of bottom wall is at $x_3^+ = 0$. ———, turbulent transport; – – –, pressure transport; —·—, SGS transport; △, viscous diffusion; □, viscous dissipation; ◇, SGS dissipation; ×, production by mean shear; +, C-L (Langmuir) forcing; ○, sum of all terms.

describing the transfer of energy between TKE components in Langmuir turbulence and summarizing the dominant budgets of TKE and 1–3 component of resolved Reynolds stress, this study provides a potential guideline for parameterizing the TKE and Reynolds stresses in general circulation models of shallow coastal regions and estuaries. Currently, none of the parameterizations often used in these models take into account the effects of Langmuir turbulence.

Figures 14(a, b) contrasts budgets of TKE in the flows with and without LC near the surface. In the flow with LC, the C-L vortex force acts as a source of TKE,

reaching a maximum at the top surface and is mostly balanced by a negative pressure transport. In this case, the pressure in the pressure transport term is affected through the C-L forcing as seen in (2.2). In the case with no LC, pressure transport is nearly zero given that there is no C-L forcing. Furthermore, production of TKE by mean shear decays faster with distance away from the surface in the flow with LC compared to that in the flow without LC. This is attributable to homogenization of mean streamwise velocity by LC. The remainder of the terms in the two cases show only slight differences.

Near the bottom, the transport of TKE follows similar dynamics in the two cases, as depicted by figures 14(c) and 14(d). The main difference is the presence of the C-L vortex force acting as a sink in the flow with LC. This sink is partially balanced by pressure transport. In the flow without LC (figure 14c), the C-L vortex force is zero and thus the pressure transport is practically zero. At the wall, in both cases, viscous diffusion serves to balance viscous dissipation.

Numerous differences occur between the flows with and without LC in terms of the dynamics governing the transport of each TKE component, i.e. $\langle \bar{u}_1' \bar{u}_1' \rangle$, $\langle \bar{u}_2' \bar{u}_2' \rangle$ and $\langle \bar{u}_3' \bar{u}_3' \rangle$. The discussion below focuses only on differences involving the transfer of energy between these components as the rest of the differences are too numerous to detail.

As was shown earlier, the C-L forcing term is zero for the x_1-momentum equation, thus it is also zero in the transport equation for $\langle \bar{u}_1' \bar{u}_1' \rangle$. Consequently, there are few differences between the flows with and without LC in the near-surface and near-bottom wall budgets of $\langle \bar{u}_1' \bar{u}_1' \rangle$ (figures 15a, d and 16a, d).

In the balance of TKE (equations (D1)–(D2), Appendix D), pressure appears only as a transport term. However, in the Reynolds stress transport equations (equations (D4)–(D5)), pressure plays a dual role, appearing as a transport term as well as a redistribution term, the latter traditionally referred to as pressure–strain redistribution. As noted by Pope (2000), pressure–strain redistribution serves to redistribute energy among the three components of TKE.

The near-surface roles of pressure–strain redistribution are drastically different in the flows with and without LC, as expected owing to the presence of the C-L vortex force as well as the modification of the pressure by the C-L forcing mechanism (see equation (2.2) in the flow with LC. As can be seen in figures 15(a) and 15(d), in the near-surface region of both flows, mean shear is the main source of $\langle \bar{u}_1' \bar{u}_1' \rangle$ energy. In the flow without LC, this energy is partially transferred to $\langle \bar{u}_2' \bar{u}_2' \rangle$ via pressure–strain redistribution (figure 15b). In the flow with LC, such a transfer does not occur, as C-L Langmuir forcing acts as the primary source of $\langle \bar{u}_2' \bar{u}_2' \rangle$ energy, while pressure–strain redistribution transfers most of this energy to $\langle \bar{u}_3' \bar{u}_3' \rangle$ (figure 16e).

The dramatic difference in pressure–strain redistribution between the flows with and without LC can be further seen in the budgets of $\langle \bar{u}_3' \bar{u}_3' \rangle$ in figures 15(c) and 15(f). In the near surface region in the flow without LC, pressure–strain redistribution alternates from source to sink to source again at the surface, while primarily balancing pressure transport. Such a characteristic is not present in the flow with LC, as pressure–strain redistribution remains a source throughout the entire near-surface region, while once again primarily balancing pressure transport.

Similar to the near-surface behaviour of both flows, mean shear is the primary contributor to $\langle \bar{u}_1' \bar{u}_1' \rangle$ energy in the near-bottom wall region (figure 16a, d). Redistribution of this energy follows different dynamics in the two flows. For example (figure 16a–c), within the near-bottom buffer layer, ($10 < x_3^+ < 50$), of the flow without LC, pressure–strain redistribution extracts energy from $\langle \bar{u}_1' \bar{u}_1' \rangle$ and redistributes it to

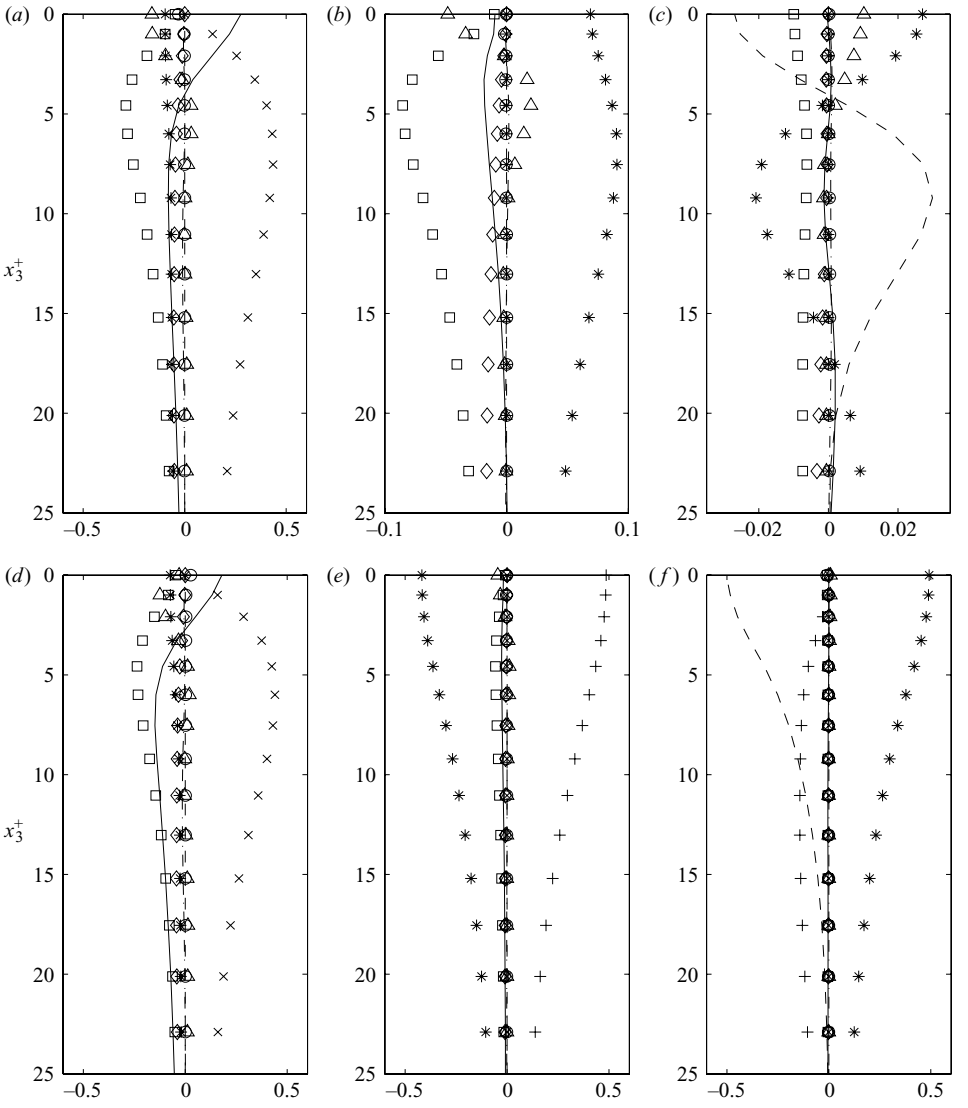

FIGURE 15. Near-top-surface budgets of TKE components in flows with (*d–f*) and without (*a–c*) LC (i.e. LC flow and no LC flow) at $Re = 395$. In flow with LC, $\lambda = 6H$ and $La_t = 0.7$. (*a*, *d*) $\langle \bar{u}_1', \bar{u}_1' \rangle$, (*b*, *e*) $\langle \bar{u}_2', \bar{u}_2' \rangle$, (*c*, *f*) $\langle \bar{u}_3' \bar{u}_3' \rangle$. Location of top surface is at $x_3^+ = 0$. *, pressure–strain redistribution; the rest of the symbols are as in figure 14. Please note that in some instances pressure–strain redistribution (denoted by '*') cannot be clearly detected as it overlaps SGS dissipation (denoted by '◇'). Also note the difference in scale of (*b*) and (*c*) as compared to the others.

$\langle \bar{u}_2' \bar{u}_2' \rangle$ and $\langle \bar{u}_3' \bar{u}_3' \rangle$. In contrast, in the flow with LC (figure 16*d–f*), pressure–strain redistribution extracts energy from $\langle \bar{u}_1' \bar{u}_1' \rangle$ and $\langle \bar{u}_3' \bar{u}_3' \rangle$ while transferring it to $\langle \bar{u}_2' \bar{u}_2' \rangle$ throughout the near-wall viscous sublayer ($x_3^+ < 10$) and buffer-layer regions.

Further differences in the near-bottom behaviour of pressure–strain redistribution between the flows with and without LC can be seen in the budgets of $\langle \bar{u}_3' \bar{u}_3' \rangle$ (figure 16*c*, *f*). In the flow without LC, within the buffer layer, pressure–strain redistribution appears as a source, while in the viscous sublayer, it appears as a sink.

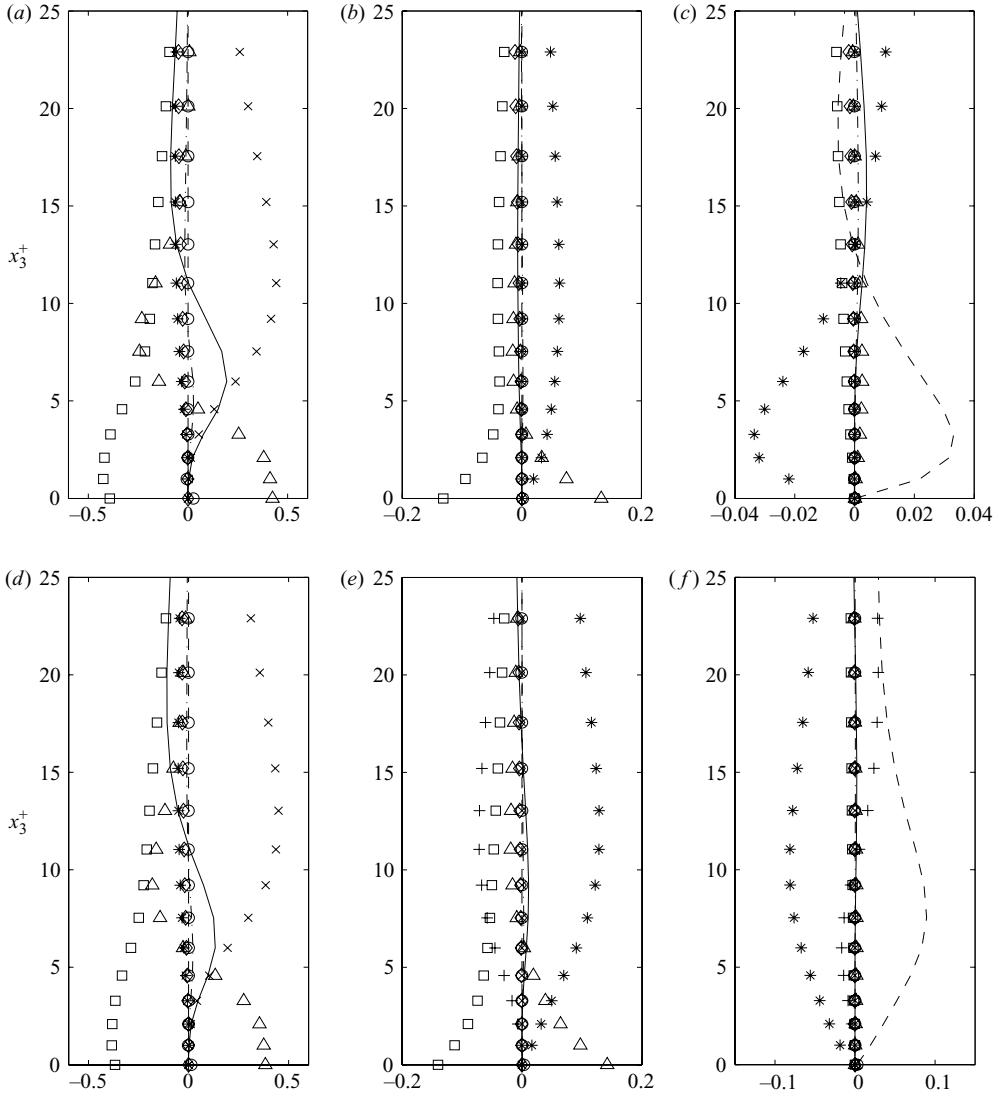

FIGURE 16. Near-bottom wall budgets of TKE components in flows with (*d–f*) and without (*a–c*) LC (i.e. LC flow and no LC flow) at $Re = 395$. In flow with LC, $\lambda = 6H$ and $La_t = 0.7$. (*a*, *d*) $\langle \bar{u}_1', \bar{u}_1' \rangle$, (*b*, *e*) $\langle \bar{u}_2', \bar{u}_2' \rangle$, (*c*, *f*) $\langle \bar{u}_3' \bar{u}_3' \rangle$. Location of bottom wall is at $x_3^+ = 0$. *, pressure–strain redistribution; the rest of the symbols as in figure 14. Please note differences in scale in the plots.

In both instances, pressure–strain redistribution serves to partially balance pressure transport. This characteristic of pressure–strain redistribution alternating from a source of $\langle \bar{u}_3' \bar{u}_3' \rangle$ in the buffer layer to a sink of $\langle \bar{u}_3' \bar{u}_3' \rangle$ in the viscous sublayer can be seen in the budgets of the turbulent channel flow simulations of Moser, Kim & Mansour (1999). Such a characteristic is not present in the flow with LC, as pressure–strain redistribution remains a sink throughout the entire near-bottom wall region, while once again primarily balancing pressure transport.

Near the surface in the flow with LC (figure 17*b*), the dominant terms in the balance of $-\langle \bar{u}_1' \bar{u}_3' \rangle$ are pressure transport (positive), C-L forcing (negative) and pressure–strain

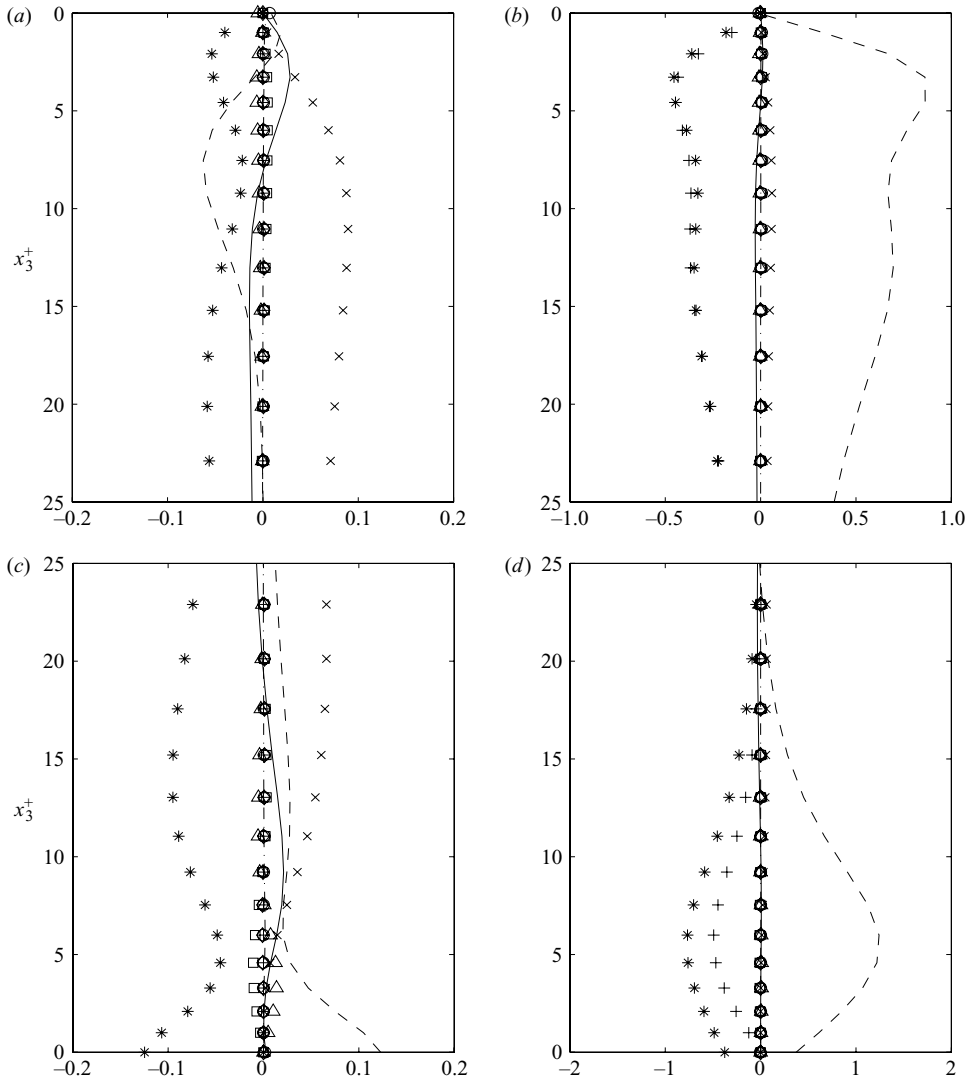

FIGURE 17. (a, b) Near-top surface and (c, d) near-bottom wall budgets of $-\langle \bar{u}_1' \bar{u}_3' \rangle$ in flows with and without LC (i.e. LC flow and no LC flow) at $Re = 395$. In flow with LC, $\lambda = 6H$ and $La_t = 0.7$. Terms are normalized by viscous scales (Pope 2000) and distances are expressed in wall units. In (a) and (b), location of top surface is at $x_3^+ = 0$. In (c) and (d) location of bottom wall is at $x_3^+ = 0$. Note the change in scale from (a) to (b) and (c) to (d).

redistribution (negative). Note that the values of C-L forcing and pressure–strain redistribution are nearly identical, causing the symbols to overlap. In contrast, in the flow without LC (figure 17*a*), production by mean shear, which is positive, is balanced by the sum of pressure transport and pressure–strain redistribution, both of which are negative. It must be noted that in the case with LC, production by mean shear is not zero, but is of the same order of magnitude as in the case without LC; thus, it is very small compared to the dominant terms. Note the change of scale in figures 17(*a*) and 17(*b*).

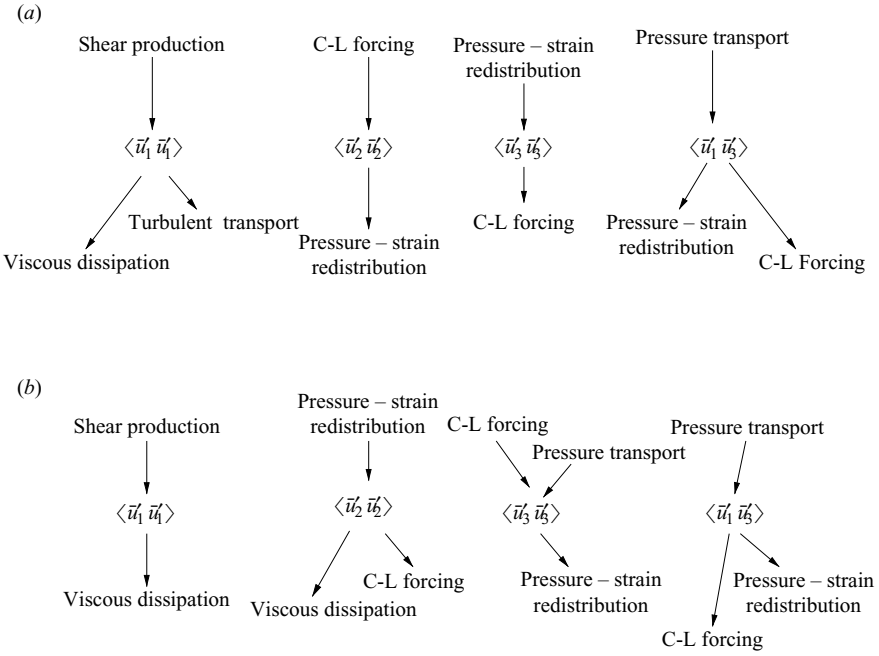

FIGURE 18. Summary of dominant terms in the transport equations for resolved Reynolds stresses in the flow with LC at $Re = 395$ ($\lambda = 6H$, $La_t = 0.7$). (*a*) Near-surface balances. (*b*) Near-bottom balances.

In the case with LC, near the wall (figure 17*d*), pressure transport serves to balance C-L forcing and pressure–strain redistribution. In this case, production by mean shear is negligible as most of the source is provided by turbulent transport. At the wall, in the case with no LC (figure 17*c*) pressure transport balances pressure–strain redistribution, as the C-L vortex force is zero. For the region $x_3^+ > 5$, production by mean shear plays a bigger role than pressure transport as they both serve to balance pressure–strain redistribution. The dominant terms are production by mean shear, pressure transport turbulent transport and pressure–strain redistribution.

It is remarkable that the near-wall and near-surface dominant budget terms of $-\langle \bar{u}_1' \bar{u}_3' \rangle$ in the flow without LC (i.e. pressure transport and pressure–strain redistribution) are an order of magnitude smaller than the corresponding near-wall dominant budget terms in the flow with LC. This disparity further demonstrates the strong impact that LC generated by intermediate waves can have on the dynamics of the turbulence in the bottom boundary layer.

Figure 18 summarizes the previously described dominant balances in the transport equations for resolved Reynolds stresses. In this figure, an arrow pointing away from a term means that term is positive in the balance and vice versa. For example, in the near-surface balance of $\langle \bar{u}_1' \bar{u}_1' \rangle$, mean shear production is positive and is balanced by two negative terms, namely viscous dissipation and turbulent transport.

3.3. *Effects of λ and La_t on Langmuir turbulence*

Next, the turbulence structure in three flows with LC are contrasted. In the first flow, the LC were generated by intermediate waves, similarly to the flow in the previous subsection. A second flow is investigated in which the LC were generated by shorter waves (corresponding to a smaller value of λ) in addition to a third flow in which

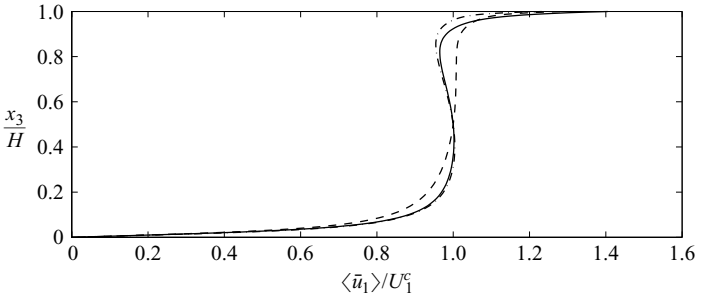

FIGURE 19. Profiles of mean velocity (normalized by U_1^c) for flows with LC at $Re = 180$. ———, flow with $\lambda = 6H$ and $La_t = 0.7$; – – –, flow with $\lambda = (4/3)H$ and $La_t = 0.7$; — · —, flow with $\lambda = 6H$ and $La_t = 0.4$.

the LC were generated by waves of greater amplitude (corresponding to a smaller value of La_t). The three flows are characterized as follows. In the first flow, $\lambda = 6H$ and $La_t = 0.7$. In the second flow, $\lambda = (4/3)H$ and $La_t = 0.7$, and in the third flow, $\lambda = 6H$ and $La_t = 0.4$. As discussed in Appendix A, preliminary tests did not show major differences between flows with LC at $Re = 180$ and $Re = 395$, both with $\lambda = 6H$ and $La_t = 0.7$. Resolution requirements for the flow at $Re = 180$ are not as high as they are for the flow at $Re = 395$. Thus, in an effort to save computational time, all flows presented in this subsection were simulated at $Re = 180$. For the three cases studied here, the computational domain was $(L_1/\delta, L_2/\delta, L_3/\delta) = (4\pi, 8\pi/3, 2)$ with a $(32 \times 64 \times 97)$ grid and grid stretching parameter $b = 0.923$.

Recall that the C-L vortex force in the governing equations is inversely proportional to La_t^2, thus a decrease in La_t leads to an increase in the overall magnitude of the C-L force throughout the water column. Furthermore, the magnitude of the C-L force is at its maximum at the top surface and decreases with depth. The decay rate is inversely proportional to λ, thus higher values of λ lead to a higher overall magnitude of the C-L force.

Mean streamwise velocity profiles for the three flows with LC are compared in figure 19. As expected, the LC in the flow with $\lambda = (4/3)H$ do not homogenize the mean velocity as far down in the water column as in the flows with $\lambda = 6H$. Consequently, the bottom boundary layer is thicker in the flow with $\lambda = (4/3)H$. In the lower half of the water column, above the bottom boundary layer, the velocity profiles for the flows with $\lambda = 6H$ look nearly identical, however, the flow with $La_t = 0.4$ does possess lower values of mean vertical shear owing to the homogenizing action of the stronger LC. Most of the impact due to different La_t is seen near the surface where the mean velocity in the flow with $La_t = 0.4$ and $\lambda = 6H$ is characterized by a slightly more negative gradient than the mean velocity in the flow with $La_t = 0.7$ and $\lambda = 6H$.

The homogenizing action of the LC in the flow with $La_t = 0.4$ extends closer to the top surface, thus the surface boundary layer in this flow is thinner.

Figures 20(a) and 20(b) show resolved normal Reynolds stress components in the flows with $\lambda = (4/3)H$ and $\lambda = 6H$, respectively. In both flows, $La_t = 0.7$. In terms of these stress components, both flows behave similarly in the near-surface region of the water column. In the lower portion of the water column, the flow with $\lambda = (4/3)H$ exhibits a behaviour closer to that of shear-dominated turbulence, for which $\langle \bar{u}_1' \bar{u}_1' \rangle$ is much greater than $\langle \bar{u}_2' \bar{u}_2' \rangle$ and $\langle \bar{u}_3' \bar{u}_3' \rangle$. This is clearly seen in figure 21(a), in terms of the Lumley invariants.

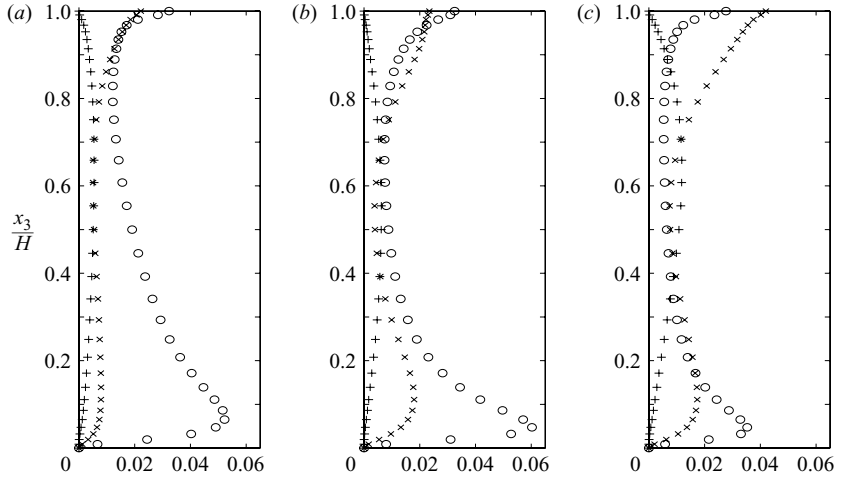

FIGURE 20. Profiles of resolved normal Reynolds stresses for flows with LC at $Re = 180$. (*a*) Flow with $\lambda = (4/3)H$ and $La_t = 0.7$. (*b*) Flow with $\lambda = 6H$ and $La_t = 0.7$. (*c*) Flow with $\lambda = 6H$ and $La_t = 0.4$. Symbols are as in figure 10(*a*). For clarity, every third point of the discrete profiles is plotted.

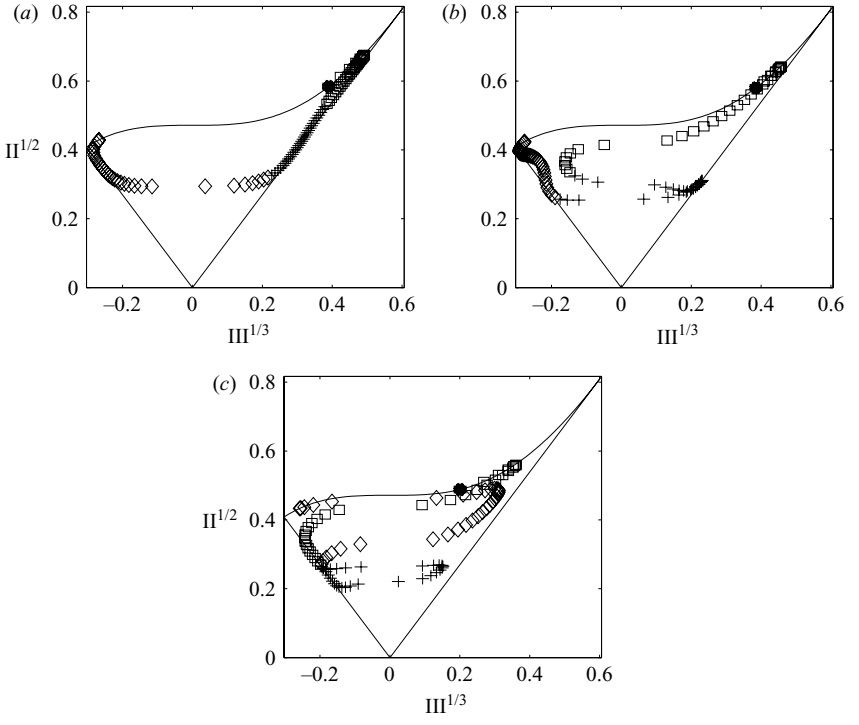

FIGURE 21. Lumley invariant maps for flows with LC at $Re = 180$. Symbols are as in figure 13. (*a*) Flow with $\lambda = (4/3)H$ and $La_t = 0.7$; (*b*) $\lambda = 6H$ and $La_t = 0.7$; (*c*) $\lambda = 6H$ and $La_t = 0.4$.

Figures 20(*b*) and 20(*c*) show resolved normal Reynolds stress components in the flows with $La_t = 0.7$ and $La_t = 0.4$, respectively. In both flows, $\lambda = 6H$. Throughout the entire water column, the flow with $La_t = 0.4$ possesses smaller values of $\langle \bar{u}_1' \bar{u}_1' \rangle$ than the flow with $La_t = 0.7$. This is due to the weaker mean vertical shear in the

flow with $La_t = 0.4$ occurring throughout most of the water column. Furthermore, lowering La_t from 0.7 to 0.4, thereby increasing the strength of Langmuir forcing leads to higher values of $\langle \bar{u}_2' \bar{u}_2' \rangle$ and $\langle \bar{u}_3' \bar{u}_3' \rangle$ in the upper half of the water column. This is expected, as an increase in Langmuir forcing leads to an increase in the production of these two components, which may be confirmed via the near-surface budget terms in the transport equations for resolved TKE components in figure 15.

Lowering the turbulent Langmuir number from $La_t = 0.7$ to $La_t = 0.4$ with fixed wavelength at $\lambda = 6H$, leads to great changes in the anisotropy of the resolved Reynolds stresses (figure 20*b*, *c*). In the flow with $La_t = 0.7$, $\langle \bar{u}_1' \bar{u}_1' \rangle$ is the largest of the normal stresses, except for the region $0.75 < x_3/H < 0.97$, where $\langle \bar{u}_2' \bar{u}_2' \rangle$ is greater. In contrast, in the flow with $La_t = 0.4$, $\langle \bar{u}_2' \bar{u}_2' \rangle$ is the largest of the normal components in the upper 25 % of the water column. Furthermore, $\langle \bar{u}_3' \bar{u}_3' \rangle$ is the largest of the normal components in the region $0.45 < x_3/H < 0.7$. Consequently, the Lumley invariant maps for these two flows (figures 21*b* and 21*c*) behave differently, especially in the upper third of the water column. Note that in the lower two-thirds of the water column, the $La_t = 0.7$ and $La_t = 0.4$ simulations, both with $\lambda = 6H$, yield Lumley invariant maps consistent with those of the observations of Part 1. Unfortunately, the upper third of the water column was not accessible in the observations, thus a comparison between simulations and observations is not possible for this portion of the water column.

In summary, for a fixed turbulent Langmuir number, La_t, the longer the waves generating LC, the stronger the impact of LC is on the structure of the turbulence in the lower portion of the water column. For LC generated by relatively shorter waves, the structure of the turbulence in the lower portion of the water column is similar to that of classical shear turbulence. Such LC only affect the turbulence structure in the upper portion of the water column. Furthermore, changing La_t from 0.7 to 0.4 in the flow with LC generated by intermediate waves with $\lambda = 6H$ leads to a re-ordering of the resolved normal Reynolds stress components and thus a different turbulent structure, especially in the upper half of the water column.

4. Discussion and conclusions

Numerous LES of LC in a wind-driven shear current in constant-density water with a non-negligible bottom boundary layer (i.e. LC in shallow water) were performed. Previous simulations of LC have been limited to deep water, where the bottom boundary layer is unimportant. The flows with LC were governed by the space and time filtered incompressible Navier–Stokes equations augmented by the C-L vortex force, often referred to as the C-L equations. The C-L vortex force models the interaction between the Stokes drift velocity, induced by the filtered-out surface gravity waves, and the shear current, thereby giving rise to LC.

Results of a shear flow without LC and the same flow with LC, the latter driven by wave- and wind-forcing conditions representative of the observations in Part 1, demonstrated the strong impact that the Langmuir cells can have on the structure of turbulent velocity fluctuations. The wind-driven shallow-water flow without LC contained velocity fluctuations characterized by large-scale streaks highly elongated in the downwind direction and alternating in sign in the crosswind direction. Such large-scale streaks had been previously discovered by Lee & Kim (1991) and Papavassiliou & Hanratty (1997) via direct numerical simulations of turbulent Couette flow. Forcing wind-driven shallow-water flow with the C-L vortex force led to larger streaks with a

characteristic crosswind length scale consistent with those recorded in the observations of Langmuir supercells (LSC) in Part 1. Visualizations of this flow on a plane normal to the wind direction, in addition to spanwise and crosswind autocorrelations of velocity fluctuations at different depths, showed that the larger streaks generated by the C-L force possessed a vertical structure also consistent with the observations of LSC. These diagnostics showed that the C-L force led to the formation of surface-intensified coherent streamwise vortices characterizing partially averaged velocity fluctuations defined as $\bar{v}_i'(x_2, x_3) = \langle \bar{u}_i' \rangle_{tx_1}$. Surface intensification of the vortices was evident through the surface-intensified converging $\bar{v}_2'$. Crosswind regions of positive (negative) $\bar{v}_1'$ coincided with crosswind regions of negative (positive) $\bar{v}_3'$, the latter referred to as downwelling limbs (upwelling limbs). Crosswind regions of positive and negative $\bar{v}_1'$ extended throughout the entire water column and even into the buffer layer within the viscous wall region, as shown by the autocorrelations. The partially averaged downwind component, $\bar{v}_1'$, exhibited near-bottom intensification, in agreement with observations. Furthermore, the ratio of the crosswind length of upwelling limbs to the crosswind length of downwelling limbs was in agreement with observed values. None of these features were present in the vertical structure of the turbulent shear flow without LC.

Further differences between the flows with and without LC were seen in terms of the resolved Reynolds stress tensor and its state of anisotropy. Differences were seen throughout the entire water column, but more importantly in the bottom third of the water column. The flow without LC exhibited a behaviour typical of shear-dominated turbulent flows in which the downwind component of the resolved normal Reynolds stress is much larger than the other two components, often referred to as axisymmetric cigar-shaped turbulence. The flow with LC behaved differently as the crosswind component of the resolved normal Reynolds stress was larger, thereby leading the turbulence towards an axisymmetric pancake-shaped state in which the downwind and crosswind components are much greater than the vertical component. This tendency towards a pancake-shaped state was also exhibited by the turbulence measured in Part 1. Even more remarkably, this tendency was seen only in the LES of the flow with LC generated by intermediate waves representative of the field observations. This tendency was not the case in a second LES of a flow with LC generated by shorter waves.

The previously summarized results are encouraging and suggest further avenues of research. Better agreement between observed and LES-predicted turbulence statistics could be pursued. Including rotational effects could potentially lead to better agreement; however, this is not likely to occur with the present numerical discretization which only permits periodicity in the horizontal directions, thus it is an unbounded horizontal domain. Instead, a bounded horizontal domain and thus a different discretization would have to be considered in order to represent accurately rotational effects in the presence of the nearby coastal boundary, which is the situation in which the measurements in Part 1 were taken. An avenue more likely to lead to better agreement between observations and simulations would be performing LES in quasi-equilibrium in which a time-varying pressure gradient is incorporated into the governing equations in order to represent the tidal component of the velocity as well as the pressure-driven geostrophic component of the velocity parallel to the coast, suggested in Part 1. In conclusion, despite the constraints of the present LES in trying to approximate field conditions, numerous characteristic features observed in LSC were reproduced numerically.

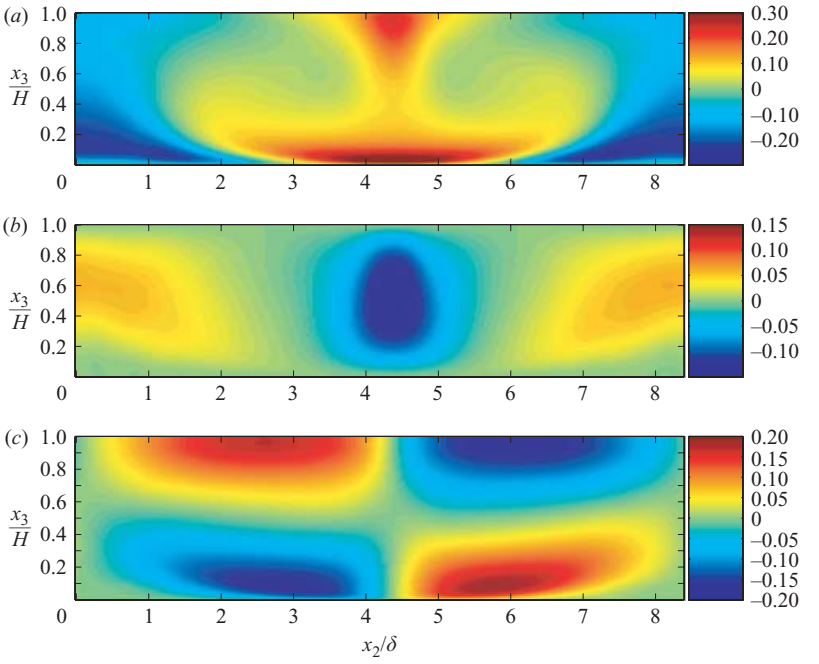

FIGURE 22. Colour maps of partially averaged fluctuating velocity components (normalized by U_1^c) on the (x_2, x_3)-plane for flow with LC generated by intermediate waves (i.e. $\lambda = 6H$) with $La_t = 0.7$ at $Re = 180$. (*a*) $\bar{v}_1'/U_1^c$, (*b*) $\bar{v}_3'/U_1^c$, (*c*) $\bar{v}_2'/U_1^c$. See figure 3 for colour maps corresponding to the same flow but with $Re = 395$.

This work was supported by the National Science Foundation under Grant OCE-0136403.

Appendix A. Effects of Reynolds number

As mentioned earlier, the Reynolds number of the field observations is much greater than that of the simulations. In the observations, $Re = O(50\,000\text{–}100\,000)$, whereas in the simulations previously discussed, $Re = 395$. In order to verify that the main characteristics of these simulations were not adversely affected by low-Reynolds-number effects, a simulation of flow with LC generated by intermediate waves with $La_t = 0.7$ at $Re = 180$ was carried out. The dimensions of the computational domain were $(L_1/\delta, L_2/\delta, L_3/\delta) = (4\pi, 8\pi/3, 2)$ and the grid was $(32 \times 64 \times 97)$ with $b = 0.923$.

Figure 22 shows the vertical/crosswind structure of partially averaged fluctuating velocity components (i.e. $\bar{v}_i'$) normalized by the mean streamwise velocity at mid-depth, U_1^c. The major features observed are very similar to those of $\bar{v}_i'$ in the flow at $Re = 395$, shown in figure 3. The main difference occurs in the ratio of the spanwise length of the upwelling limb to the spanwise length of the downwelling limb, r. In the flow at $Re = 180$, the mid-depth value of r is 1.6, whereas in the flow at $Re = 395$, this value is 1.4. The latter ratio is in closer agreement with the ratios of 1.1–1.3 reported in the observations (Part 1). A lower value of r at higher Reynolds number can be attributed to the resolved turbulent kinetic energy (TKE) at the surface. In the flow at higher Reynolds number, TKE at the surface is greater, thereby generating greater

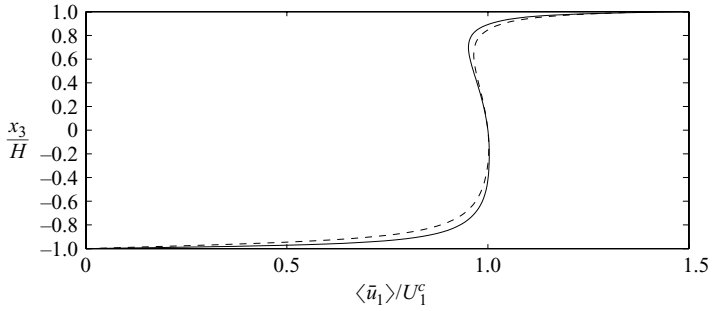

FIGURE 23. Mean downwind velocity profiles (normalized by U_1^c) for flows with LC generated by intermediate waves (i.e. $\lambda = 6H$) with $La_t = 0.7$ at different Reynolds numbers. ———, flow at $Re = 395$; - - -, flow at $Re = 180$.

mixing there. Because the downwelling limb is generated at the surface, it is more intensely mixed in the flow at higher Re and thus more diffuse. Owing to conservation of mass, a more diffuse downwelling limb leads to a less diffuse upwelling limb, and thus a lower value of r.

In addition to the similar structure of the Langmuir cells, there are other major characteristics of the flows at $Re = 180$ and $Re = 395$ that are similar. For example, the ordering of the resolved normal Reynolds stresses for the flow at $Re = 395$ (figure 10a) follows the same ordering in the lower, middle and upper thirds of the water column, as in the flow at $Re = 180$ (figure 20a). Consequently, the trajectory of the Lumley invariant map is similar for both flows (cf. figures 13a and 21b).

Figure 23 compares the mean streamwise velocity for the flows at $Re = 180$ and $Re = 395$. The main difference between these velocity profiles is the slope at the bottom. Because the flow at higher Re is driven by a higher stress at the surface, the vertical gradients of the velocity at the top surface and at the bottom wall are greater. Additionally, the velocity profile in the flow at $Re = 395$ is better mixed above the bottom boundary layer, as expected in a flow with higher Re.

Appendix B. Domain size

In order to verify that the resolution of a single Langmuir cell does not have an adverse impact on the results, a second simulation of the flow with LC generated by intermediate waves with $La_t = 0.7$ at $Re = 180$ was performed in a domain with a spanwise length twice that of the earlier simulation. The earlier simulation was performed in a domain with $L_2/\delta = 8\pi/3$ and the current simulation was performed with $L_2/\delta = 16\pi/3$; in both simulations, $L_1/\delta = 4\pi$. The earlier simulation was performed on a $(32 \times 64 \times 97)$ grid while the current simulation was performed on a $(32 \times 128 \times 97)$ grid; in both simulations, $b = 0.923$. Because the spanwise domain length was twice that in the current simulation, it required twice the number of grid points in x_2 to preserve the grid resolution.

Figure 24 depicts the vertical/crosswind structure of partially averaged fluctuating velocity components, $\bar{v}_i'$ (normalized by U_1^c), associated with Langmuir cells. The expanded computational domain contains two Langmuir cells, compared to the original domain in which one cell was resolved. Thus, increasing the spanwise computational domain length did not trigger a re-sizing of the single-cell structure previously obtained so as to re-occupy the expanded domain. The mid-depth ratio of

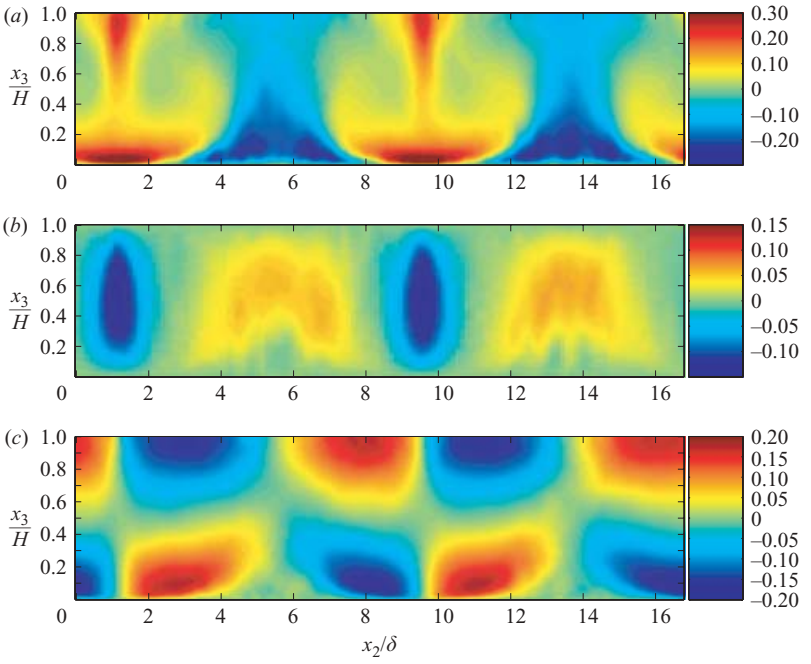

FIGURE 24. Colour maps of partially averaged fluctuating velocity components (normalized by U_1^c) on the (x_2, x_3)-plane for flow with LC generated by intermediate waves (i.e. $\lambda = 6H$), $La_t = 0.7$, $Re = 180$ and expanded crosswind domain length ($L_2/\delta = 16\pi/3$). (*a*) $\bar{v}_1'/U_1^c$, (*b*) $\bar{v}_3'/U_1^c$, (*c*) $\bar{v}_2'/U_1^c$. See figure 22 for colour maps corresponding to same flow but with $L_2/\delta = 8\pi/3$.

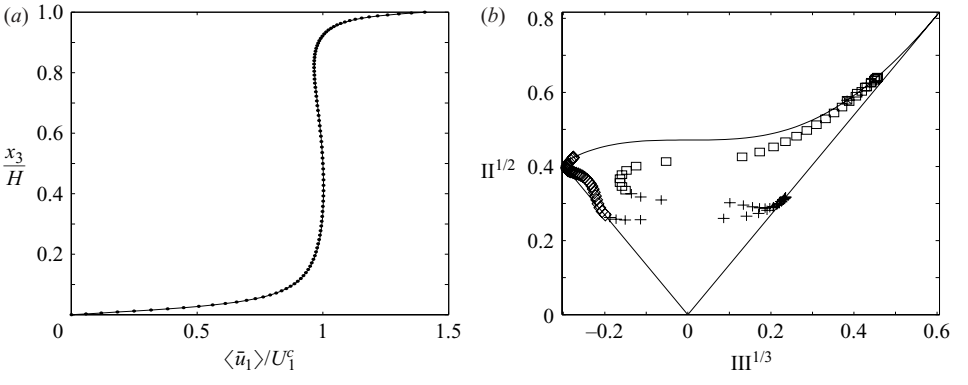

FIGURE 25. (*a*) Mean downwind velocity profiles (normalized by U_1^c) in flows with LC generated by intermediate waves (i.e. $\lambda = 6H$) with $La_t = 0.7$, $Re = 180$ and different crosswind domain length L_2/δ. (*b*) Lumley invariant map for flow with $L_2/\delta = 16\pi/3$. See figure 21(*c*) for a map corresponding to same flow but with $L_2/\delta = 8\pi/3$. In (*a*) ———, $L_2/\delta = 16\pi/3$; - - -, $L_2/\delta = 8\pi/3$.

the spanwise length of the upwelling limbs to the spanwise length of the downwelling limbs is approximately 1.6, just as it was in the earlier simulation.

Further results of the simulation with the expanded spanwise domain can be seen in figure 25. Hardly any difference is seen between the original simulation and the current one in terms of mean velocity and Lumley invariant maps.

Appendix C. Effects of grid cell size and subgrid-scale closure

This section presents studies exploring effects of grid cell size (or grid resolution) and subgrid-scale (SGS) closure on the results of LES in flow with LC generated by intermediate waves with $La_t = 0.7$. The effects of grid resolution and SGS closure are discussed in the same section because they are related to one another. As grid resolution is increased, the impact of the SGS closure weakens. Additionally, it is expected that effects due to grid resolution and subgrid-scale closure have a stronger impact on the LC flow at $Re = 180$ with the $(32 \times 64 \times 97)$ grid than on the LC flow at $Re = 395$ with the $(96 \times 96 \times 97)$ grid because of the coarser resolution in the former. Thus, results shown in this section were obtained with LC flow at $Re = 180$.

Simulation results obtained with the dynamic Smagorinsky closure discussed in § 2.2 and the dynamic mixed closure of Morinishi & Vasilyev (2001) are compared. In the latter closure, the deviatoric part of the SGS stress is computed as

$$\tau_{ij}^d = C_L(\bar{\bar{u}}_i\bar{\bar{u}}_j - \overline{\bar{u}_i\bar{u}_j})^d + 2(C_s\bar{\Delta})^2|\bar{S}|\bar{S}_{ij}. \tag{C 1}$$

In the former closure, τ_{ij}^d is given by (2.6). The coefficient $(C_s\bar{\Delta})^2$ in (C 1) is computed dynamically in the same way as before in (2.7). The coefficient C_L is computed dynamically as

$$C_L = \frac{\langle [L_{ij} + 2(C_s\bar{\Delta})^2 M_{ij}] H_{ij}^d \rangle}{\langle H_{kl}^d H_{kl}^d \rangle}, \tag{C 2}$$

where L_{ij} and M_{ij} are specified in (2.8) and (2.9), respectively, and

$$H_{ij} = (\widehat{\bar{\hat{u}}_i\bar{\hat{u}}_j} - \hat{\bar{\hat{u}}}_i\hat{\bar{\hat{u}}}_j) - (\widehat{\bar{u}_i\bar{u}_j} - \hat{\bar{u}}_i\hat{\bar{u}}_j). \tag{C 3}$$

Recall that the hat notation $\hat{\cdot}$, denotes application of a test filter over the horizontal directions of the flow, as discussed in § 2.2. The bar notation, $\bar{\cdot}$, denotes application of the grid filter, implicitly set by the numerical method. Knowledge of the grid filter, or at least an approximation to the grid filter, is required in order to compute the tensor H_{ij}. As an approximation to grid filtering, the following operation suggested by Morinishi & Vasilyev is used:

$$\bar{f}(x_i^*) = \tfrac{1}{24}[f(x_i^* - h_i) + 22f(x_i^*) + f(x_i^* + h_i)], \tag{C 4}$$

where $\bar{f}(x_i^*)$ is the function f filtered over the x_i-direction evaluated at $x_i = x_i^*$ and h_i is the grid cell size in the x_i-direction. The width characterizing the filter induced by the operation in (C 4) is $\bar{\Delta}_i = h_i$. In the current implementation, the filter operation in (C 4) was applied over periodic directions of the flow (x_1 and x_2).

Before studying the effects of grid resolution and SGS closure, it is worth considering the Reynolds-averaged governing equations. Using the continuity equation, the viscous term in the momentum equation in (2.1) may be expressed as

$$\frac{1}{Re}\frac{\partial^2\bar{u}_i}{\partial x_j^2} = \frac{\partial\tau_{ij}^v}{\partial x_j}, \tag{C 5}$$

where the viscous stress is

$$\tau_{ij}^v = \frac{1}{Re}\left(\frac{\partial\bar{u}_i}{\partial x_j} + \frac{\partial\bar{u}_j}{\partial x_i}\right). \tag{C 6}$$

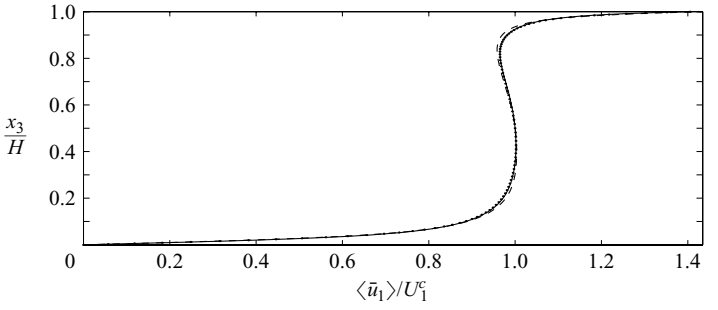

FIGURE 26. Profiles of mean velocity (normalized by U_1^c) for flows with LC at $Re = 180$ ($\lambda = 6H$, $La_t = 0.7$) with different grid resolutions and subgrid-scale closures. - - -, simulation on ($32 \times 64 \times 97$) grid with dynamic Smagorinsky closure; ———, simulation on ($48 \times 96 \times 145$) grid with dynamic Smagorinsky closure; – – –, simulation on ($32 \times 64 \times 97$) grid with dynamic mixed closure.

Using the decomposition in (3.1) and equations (C 5) and (C 6), the x_1-momentum equation becomes

$$f(x_3) = -\frac{\mathrm{d}\langle \bar{u}_1' \bar{u}_3' \rangle}{\mathrm{d}x_3} + \frac{\mathrm{d}\langle \tau_{13}^d \rangle}{\mathrm{d}x_3} + \frac{\mathrm{d}\langle \tau_{13}^v \rangle}{\mathrm{d}x_3} = 0. \tag{C 7}$$

Integrating the previous expression in x_3 leads to

$$g(x_3) = -\langle \bar{u}_1' \bar{u}_3' \rangle + \langle \tau_{13}^d \rangle + \langle \tau_{13}^v \rangle = C, \tag{C 8}$$

where C is a constant. This constant can be determined by evaluating function $g(x_3)$ at the bottom wall (at $x_3 = 0$). At $x_3 = 0$, the 1–3 component of the resolved Reynolds stress tensor ($\langle \bar{u}_1' \bar{u}_3' \rangle$) and the 1–3 component of the subgrid-scale stress tensor (τ_{13}^d) both vanish. Thus, C is equal to the averaged 1–3 component of the viscous stress tensor at the bottom wall (i.e. $C = \langle \tau_{13}^v \rangle|_{x_3=0}$). Note that the 1–3 component of the subgrid-scale stress tensor and all of the other components of this tensor vanish at the bottom wall for both the dynamic Smagorinsky closure and the dynamic mixed closure. Now that C has been determined, (C 8) may be re-expressed as

$$\frac{g(x_3)}{\langle \tau_{13}^v \rangle|_{x_3=0}} = -\frac{\langle \bar{u}_1' \bar{u}_3' \rangle}{\langle \tau_{13}^v \rangle|_{x_3=0}} + \frac{\langle \tau_{13}^d \rangle}{\langle \tau_{13}^v \rangle|_{x_3=0}} + \frac{\langle \tau_{13}^v \rangle}{\langle \tau_{13}^v \rangle|_{x_3=0}} = 1. \tag{C 9}$$

Note that satisfaction of (C 7) serves as an indicator for turbulence under statistical equilibrium. For the flow configurations with and without LC, global conservation of streamwise momentum implies that the plane-averaged bottom stress should be equal to the prescribed surface stress (in the temporal mean). In all the cases presented in this paper, temporal/plane averages of turbulent quantities were collected once the plane-averaged bottom stress normalized by τ_s was close to one (in the temporal mean) throughout several flow-throughs. These averages were collected over a sufficiently long time period such that the relation in (C 7) was satisfied. Averaging over longer time periods resulted in nearly indistiguishable temporal/horizontal averages of turbulent quantities, thereby signalling that the turbulence had reached a statistical equilibrium.

Figures 26 and 27 compare mean streamwise velocity and resolved normal Reynolds stress components for three simulations all with LC generated by intermediate waves, $La_t = 0.7$ and $Re = 180$. One of the simulations was performed with the dynamic Smagorinsky closure, and another with the dynamic mixed closure, both on the

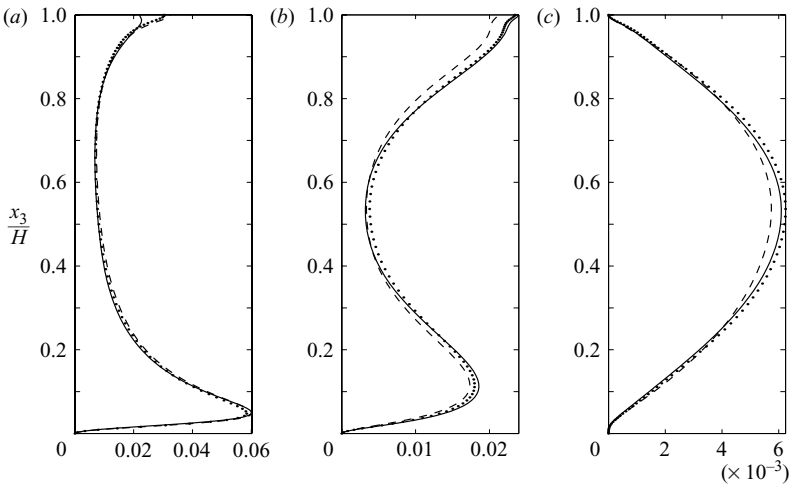

FIGURE 27. Resolved normal Reynolds stress components (normalized by U_1^{c2}) for flow with LC at $Re = 180$ ps ($\lambda = 6H$, $La_t = 0.7$) with different grid resolutions and subgrid-scale closures. (*a*) $\langle \bar{u}_1' \bar{u}_1' \rangle / U_1^{c2}$, (*b*) $\langle \bar{u}_2' \bar{u}_2' / U_1^{c2}$, (*c*) $\langle \bar{u}_3' \bar{u}_3' \rangle / U_1^{c2}$. - - -, simulation on (32×64×97) grid with dynamic Smagorinsky closure; ———, simulation on ($48 \times 96 \times 145$) grid with dynamic Smagorinsky closure; – – –, simulation on ($32 \times 64 \times 97$) grid with dynamic mixed closure.

($32 \times 64 \times 97$) grid with $b = 0.923$ discussed earlier. A third simulation was performed with the dynamic Smagorinsky closure, but on a finer ($48 \times 96 \times 145$) grid with $b = 0.859$. Mean streamwise velocity profiles (figure 26) are nearly indistinguishable in the three simulations. The simulations with equal resolution and different subgrid-scale closures predict values of $\langle \bar{u}_1' \bar{u}_1' \rangle$ very close to each other. In terms of $\langle \bar{u}_2' \bar{u}_2' \rangle$, the simulation with the dynamic mixed closure predicts slightly lower values, especially in the upper and lower sections of the water column (figure 27*b*). In terms of $\langle \bar{u}_3' \bar{u}_3' \rangle$, the simulation with the dynamic mixed closure predicts slightly lower values, especially in the middle of the water column. These differences between the results with dynamic Smagorinsky and dynamic mixed closures are negligible. Most of the differences between the simulations with the dynamic Smagorinsky closure at different resolutions are negligible as well, thus verifying that the simulation on the coarser grid was not adversely affected by grid size. The main difference between the simulations with the dynamic Smagorinsky closure at different resolutions is in the predicted value of $\langle \bar{u}_1' \bar{u}_1' \rangle$ at the top surface. The simulation at coarser resolution overpredicts $\langle \bar{u}_1' \bar{u}_1' \rangle$ by about 10 % relative to the simulation at finer resolution. This is attributable to the effect of the SGS closure which is greatest near the top surface. The impact of the SGS closure is greatly reduced with grid refinement, as will be shown next.

Figure 28 shows the dominant shear components (i.e. the 1–3 components) of resolved Reynolds stress, viscous stress and subgrid-scale stress in the three simulations previously discussed. In the simulation with the dynamic Smagorinsky closure, the 1–3 component of the subgrid-scale stress is given as $\tau_{13}^d = 2\nu_T \bar{S}_{13}$ where the eddy viscosity, ν_T, was defined in (2.6) and $\bar{S}_{13} = (\bar{u}_{1,3} + \bar{u}_{3,1})/2$. As discussed earlier, the presence of Langmuir circulations causes homogenization of the streamwise velocity in the middle of the water column. Consequently, the presence of the Langmuir circulations reduces the magnitude of $\bar{S}_{13}$ and thus of τ_{13}^d to nearly zero, especially in the middle third of the water column (figure 28*a*). In the case of the dynamic mixed model, τ_{13}^d is not affected as much by homogenization of streamwise velocity

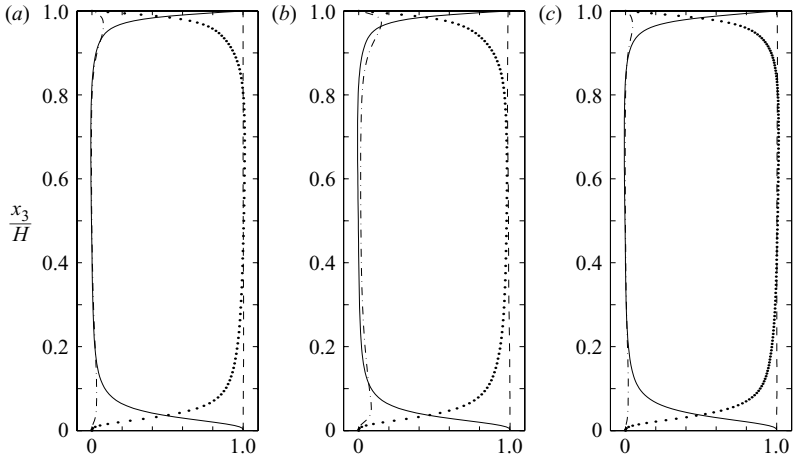

FIGURE 28. Mean dominant shear (1–3) component of resolved Reynolds stress, viscous stress and subgrid-scale stress for flows with LC $Re = 180$ ($\lambda = 6H$, $La_t = 0.7$) with different grid resolutions and subgrid-scale closures. (*a*) Simulation on ($32 \times 64 \times 97$) grid with dynamic Smagorinsky closure; (*b*) simulation on ($32 \times 64 \times 97$) grid with dynamic mixed closure; (*c*) simulation on ($48 \times 96 \times 145$) grid with dynamic Smagorinsky closure. - - -, 1–3 component of resolved Reynolds stress (i.e. $-\langle \bar{u}'_1 \bar{u}'_3 \rangle$); ———, 1–3 component of mean viscous stress (i.e. $(1/Re)\,\mathrm{d}\langle \bar{u}_1 \rangle / \mathrm{d}x_3$); — · —, 1–3 component of mean subgrid-scale stress (i.e. $\langle \tau^d_{13} \rangle$); - - -, sum of previous three quantities. All quantities are normalized by the value of $\langle \tau^v_{13} \rangle$ at the bottom wall (i.e. $\langle \tau^v_{13} \rangle|_{x_3 = 0}$).

because it is not solely proportional to $\bar{S}_{13}$ (see (C 1)). In the middle third of the water column (figure 28*a*, *b*), τ^d_{13} given by the dynamic mixed closure is greater than τ^d_{13} given by the dynamic Smagorinsky closure. In both simulations with the different subgrid-scale closures, the presence of Langmuir cells also tends to drive the 1–3 component of the mean viscous stress (i.e. $\langle \tau^v_{13} \rangle = \langle \bar{u}_{1,3} \rangle / Re$) close to zero. Taking this into consideration together with the relation in (C 7), higher values of $\langle \tau^d_{13} \rangle$ lead to lower values of $-\langle \bar{u}'_1 \bar{u}'_3 \rangle$ when comparing the simulation using the dynamic mixed closure to its counterpart using the dynamic Smagorinsky closure. Note that for both of these simulations as well as for the simulation at greater resolution, the relation in (C 9) is satisfied throughout the entire water column.

Comparing the simulations using the dynamic Smagorinsky closure at different resolutions (figure 28*a*, *c*), shows that refining the grid leads to a reduction of $\langle \tau^d_{13} \rangle$, which is a well-known attribute of the dynamic closure. This reduction is appreciable in regions near the bottom wall and near the top surface where values of $\langle \tau^d_{13} \rangle$ are larger than elsewhere.

Appendix D. Transport equations

D.1. *Resolved Reynolds stress*

Following the Reynolds decomposition, $\bar{u}_i = \langle \bar{u}_i \rangle + \bar{u}'_i$, the transport equation for the mean resolved Reynolds stress tensor, $\langle \bar{u}'_i \bar{u}'_j \rangle$, can be written as

$$\frac{\partial}{\partial t}\langle \bar{u}'_i \bar{u}'_j \rangle + \langle \bar{u}_k \rangle \frac{\partial}{\partial x_k}\langle \bar{u}'_i \bar{u}'_j \rangle = P_{ij} + Q_{ij} + T_{ij} + T^{sgs}_{ij} + D_{ij} + A_{ij} + B_{ij} + \epsilon_{ij} + \epsilon^{sgs}_{ij}, \quad \text{(D 1)}$$

where

$$P_{ij} = -\langle \bar{u}_i' \bar{u}_k' \rangle \frac{\partial \langle \bar{u}_j \rangle}{\partial x_k} - \langle \bar{u}_j' \bar{u}_k' \rangle \frac{\partial \langle \bar{u}_i \rangle}{\partial x_k} \quad \text{(mean shear production rate)}, \tag{D 2a}$$

$$Q_{ij} = \frac{1}{La_T^2} \left[\epsilon_{jlk} \phi_l^s \langle \bar{\omega}_k' \bar{u}_i' \rangle + \epsilon_{ilk} \phi_l^s \langle \bar{\omega}_k' \bar{u}_j' \rangle \right] \quad \text{(C-L (Langmuir) forcing rate)}, \tag{D 2b}$$

$$T_{ij} = -\frac{\partial}{\partial x_k} \langle \bar{u}_i' \bar{u}_j' \bar{u}_k' \rangle \quad \text{(turbulent transport rate)}, \tag{D 2c}$$

$$T_{ij}^{sgs} = \frac{\partial}{\partial x_k} \left[\langle \bar{u}_i' \tau_{jk}^{d'} \rangle + \langle \bar{u}_j' \tau_{ik}^{d'} \rangle \right] \quad \text{(SGS transport rate)}, \tag{D 2d}$$

$$D_{ij} = \frac{1}{Re} \frac{\partial^2}{\partial x_k^2} \langle \bar{u}_i' \bar{u}_j' \rangle \quad \text{(viscous diffusion rate)}, \tag{D 2e}$$

$$A_{ij} = -\frac{\partial}{\partial x_k} [\delta_{jk} \langle \bar{\Pi}' \bar{u}_i' \rangle + \delta_{ik} \langle \bar{\Pi}' \bar{u}_j' \rangle] \quad \text{(pressure transport rate)}, \tag{D 2f}$$

$$B_{ij} = 2 \langle \bar{\Pi}' \bar{S}_{ij}' \rangle \quad \text{(pressure–strain redistribution rate)}, \tag{D 2g}$$

$$\epsilon_{ij} = -\frac{2}{Re} \left\langle \frac{\partial \bar{u}_i'}{\partial x_k} \frac{\partial \bar{u}_j'}{\partial x_k} \right\rangle \quad \text{(viscous dissipation rate)}, \tag{D 2h}$$

$$\epsilon_{ij}^{sgs} = -\left\langle \tau_{ik}^{d'} \frac{\partial \bar{u}_j'}{\partial x_k} \right\rangle - \left\langle \tau_{jk}^{d'} \frac{\partial \bar{u}_i'}{\partial x_k} \right\rangle \quad \text{(SGS dissipation rate)}. \tag{D 2i}$$

In general,

$$\langle a_{ij}' b_{kl}' \rangle = \langle a_{ij} b_{kl} \rangle - \langle a_{ij} \rangle \langle b_{kl} \rangle. \tag{D 3}$$

D.2. *Resolved turbulent kinetic energy*

Similarly, the transport equation for mean resolved turbulent kinetic energy, $\bar{q} \equiv \langle \bar{u}_i' \bar{u}_i' \rangle / 2$, can be expressed as

$$\frac{\partial \bar{q}}{\partial t} + \langle \bar{u}_k \rangle \frac{\partial \bar{q}}{\partial x_k} = P + Q + T + T^{sgs} + D + A + \epsilon + \epsilon^{sgs}, \tag{D 4}$$

where

$$P = -\langle \bar{u}_i' \bar{u}_j' \rangle \frac{\partial \langle \bar{u}_i \rangle}{\partial x_j} \quad \text{(mean shear production rate)}, \tag{D 5a}$$

$$Q = \frac{1}{La_T^2} \epsilon_{ijk} \phi_j^s \langle \bar{\omega}_k' \bar{u}_i' \rangle \quad \text{(C-L (Langmuir) forcing rate)}, \tag{D 5b}$$

$$T = -\frac{\partial}{\partial x_j} \langle \bar{q} \bar{u}_j' \rangle \quad \text{(turbulent transport rate)}, \tag{D 5c}$$

$$T^{sgs} = \frac{\partial}{\partial x_j} \langle \bar{u}_i' \tau_{ij}^{d'} \rangle \quad \text{(SGS transport rate)}, \tag{D 5d}$$

$$D = \frac{1}{Re} \frac{\partial^2 \bar{q}}{\partial x_j^2} \quad \text{(viscous diffusion rate)}, \tag{D 5e}$$

$$A = -\frac{\partial}{\partial x_j} \langle \bar{\Pi}' \bar{u}_j' \rangle \quad \text{(pressure transport rate)}, \tag{D 5f}$$

$$\epsilon = -\frac{1}{Re} \left\langle \frac{\partial \bar{u}_i'}{\partial x_j} \frac{\partial \bar{u}_i'}{\partial x_j} \right\rangle \quad \text{(viscous dissipation rate)}, \tag{D 5g}$$

$$\epsilon^{sgs} = -\langle \tau_{ij}^{d'} \bar{S}_{ij}' \rangle \quad \text{(SGS dissipation rate)}. \tag{D 5h}$$

Appendix E. Numerical method

E.1. *Temporal discretization*

The continuity and momentum equations in (2.1) are solved on a non-staggered grid using the second-order time accurate semi-implicit fractional step method analysed by Armfield & Street (2000). Fractional-step methods integrate the equations in (2.1) in a segregated manner. In other words, the momentum equations are first solved for the velocity and some form of Poisson's equation is solved for pressure. The Poisson's equation is derived using the continuity and momentum equations. Thus, solution of this equation provides the pressure and also acts to enforce continuity.

For simplicity, the advection, gradient of the subgrid-scale stress and the C-L vortex force terms are gathered into function H_i as

$$H_i(\bar{u}_k) = \bar{u}_j \frac{\partial \bar{u}_i}{\partial x_j} - \frac{\partial \tau_{ij}^d}{\partial x_j} - \epsilon_{ijk} \frac{1}{La_t^2} \phi_j^s \bar{\omega}_k. \tag{E 1}$$

Reverting to vector notation (i.e. $\bar{\boldsymbol{u}} = (\bar{u}_1, \bar{u}_2, \bar{u}_3)$, $\nabla = (\partial_{x_1}, \partial_{x_2}, \partial_{x_3})$, $\boldsymbol{H} = (H_1, H_2, H_3)$ and so on) the terms in (E 1) are explicitly discretized using the second-order time accurate Adams–Bashforth scheme as

$$\boldsymbol{N}(\bar{\boldsymbol{u}}^n, \bar{\boldsymbol{u}}^{n-1}) = \tfrac{3}{2}\boldsymbol{H}(\bar{\boldsymbol{u}}^n) - \tfrac{1}{2}\boldsymbol{H}(\bar{\boldsymbol{u}}^{n-1}), \tag{E 2}$$

where the superscripts refer to time steps n and $n-1$. Using the second-order time accurate Crank–Nicolson scheme to discretize the viscous term together with the previous Adams–Bashforth scheme, the discretized momentum equation may be re-expressed as

$$\left(\frac{1}{\Delta t} - \frac{1}{2Re}\nabla^2\right) \Delta \bar{\boldsymbol{u}}_*^{n+1} = -N(\bar{\boldsymbol{u}}^n, \bar{\boldsymbol{u}}^{n-1}) + \frac{1}{Re}\nabla^2 \bar{\boldsymbol{u}}^n - \nabla \bar{\Pi}^n \quad \text{in } \Omega, \tag{E 3a}$$

$$\boldsymbol{t}_i \cdot \bar{\boldsymbol{u}}_*^{n+1} = 0 \quad \text{for } i = 1, 2 \quad \text{on } \partial\Omega_1, \tag{E 3b}$$

$$(\boldsymbol{n} \cdot \nabla)\left(\bar{u}_{1*}^{n+1}, \bar{u}_{2*}^{n+1}\right) = (Re, 0) \quad \text{on } \partial\Omega_2, \tag{E 3c}$$

$$\bar{\boldsymbol{u}}_*^{n+1} = \bar{\boldsymbol{u}}^n + \Delta \bar{\boldsymbol{u}}_*^{n+1} \quad \text{in } \Omega + \partial\Omega. \tag{E 3d}$$

where $\bar{\boldsymbol{u}}_*^{n+1} = (\bar{u}_{1*}^{n+1}, \bar{u}_{2*}^{n+1}, \bar{u}_{3*}^{n+1})$, Δt is the time step, $\boldsymbol{n}$ is the unit normal vector to either the bottom or top boundary, $\partial\Omega_1$ denotes the bottom boundary and $\partial\Omega_2$ denotes the top boundary. Furthermore, Ω denotes the interior of the domain excluding the boundaries and $\partial\Omega$ denotes both bottom and top boundaries. Vectors $\boldsymbol{t}_1$ and $\boldsymbol{t}_2$ are linearly independent unit vectors normal to $\boldsymbol{n}$. The solution of (E 3) at time t_{n+1}, intermediate solution $\bar{\boldsymbol{u}}_*^{n+1}$, does not satisfy the continuity equation. To enforce the divergence-free condition, the following Poisson's equation for pressure is first solved:

$$\nabla^2(\Delta \bar{\Pi}^{n+1}) = \frac{1}{\Delta t}\, \nabla \cdot \bar{\boldsymbol{u}}_*^{n+1} \quad \text{in } \Omega + \partial\Omega, \tag{E 4a}$$

$$\frac{\partial \Delta \bar{\Pi}^{n+1}}{\partial \boldsymbol{n}} = \frac{1}{\Delta t}\, \boldsymbol{n} \cdot \bar{\boldsymbol{u}}_*^{n+1} \quad \text{on } \partial\Omega, \tag{E 4b}$$

$$\bar{\Pi}^{n+1} = \bar{\Pi}^n + \Delta \bar{\Pi}^{n+1} \quad \text{in } \Omega + \partial\Omega. \tag{E 4c}$$

The divergence-free velocity is finally obtained as

$$\bar{\boldsymbol{u}}^{n+1} = \bar{\boldsymbol{u}}_*^{n+1} - \Delta t\, \nabla(\Delta \bar{\Pi}^{n+1}) \quad \text{in } \Omega + \partial\Omega. \tag{E 5}$$

In (E 3*b*), the component of the intermediate velocity normal to the bottom and top boundaries (i.e. $\boldsymbol{n}\cdot\bar{\boldsymbol{u}}_*^{n+1}=\bar{u}_{3*}^{n+1}$ on $\partial\Omega$) is not specified and thus kept free as given by the solution of (E 3*a*). In turn, this free velocity affects the solution of the Poisson's equation for pressure through the boundary condition in (E 4). As discussed by Slinn & Riley (1998), this is required to ensure convergence of the method. However, at the end of the time step, when the final velocity is computed via (E 5), $\bar{u}_3^{n+1}$ is set to zero on $\partial\Omega$, thus satisfying the true boundary condition. Validation studies, not shown, demonstrated that this splitting of the momentum and continuity equation together with the chosen Adams–Bashforth and Crank–Nicolson schemes is second-order accurate in time.

E.2. *Spatial discretization*

The spatial discretization is hybrid, as it makes use of fast Fourier transforms in the horizontal direction (x_1 and x_2) and high-order finite differences in the vertical direction (x_3). Taking the two-dimensional Fourier transform of the temporally discrete momentum equation in (E 3) and denoting a Fourier transformed quantity with an over-hat, $\hat{\cdot}$, leads to

$$\left(\frac{1}{\Delta t}+\frac{1}{2Re}|\boldsymbol{k}_h|^2-\frac{1}{2Re}\frac{\delta^2}{\delta x_3^2}\right)\widehat{\Delta\bar{\boldsymbol{u}}}_*^{n+1}=-\hat{N}(\bar{\boldsymbol{u}}^n,\bar{\boldsymbol{u}}^{n-1})-\nabla_s\,\hat{\bar{\Pi}}^n + \frac{1}{Re}\left\{-|\boldsymbol{k}_h|^2+\frac{\delta^2}{\delta x_3^2}\right\}\hat{\bar{\boldsymbol{u}}}^n \quad \text{in } \Omega, \tag{E 6a}$$

$$\left(\hat{\bar{u}}_{1*}^{n+1},\hat{\bar{u}}_{2*}^{n+1}\right)=(0,0) \quad \text{on } \partial\Omega_1, \tag{E 6b}$$

$$\left(\frac{\delta\hat{\bar{u}}_{1*}^{n+1}}{\delta x_3},\frac{\delta\hat{\bar{u}}_{2*}^{n+1}}{\delta x_3}\right)=(Re,0) \quad \text{on } \partial\Omega_2, \tag{E 6c}$$

$$\hat{\bar{\boldsymbol{u}}}_*^{n+1}=\hat{\bar{\boldsymbol{u}}}^n+\widehat{\Delta\bar{\boldsymbol{u}}}_*^{n+1} \quad \text{in } \Omega, \tag{E 6d}$$

where $\boldsymbol{k}_h=k_1\boldsymbol{e}_1+k_2\boldsymbol{e}_2$ and k_1 (resp. $\boldsymbol{e}_1$) and k_2 (resp. $\boldsymbol{e}_2$) are the wavenumbers (resp. unit vectors) in the x_1 and x_2 directions. The operator $\delta/\delta x_3$ denotes the finite-difference approximation of $\partial/\partial x_3$ and $\nabla_s=(ik_1,ik_2,\delta/\delta x_3)$. Further information regarding the finite-difference operators can be found in Appendix F. Taking the two-dimensional Fourier transport of the Poisson's equation in (E 4*c*) leads to

$$\left(-|\boldsymbol{k}_h|^2+\frac{\delta^2}{\delta x_3^2}\right)\widehat{\Delta\bar{\Pi}}^{n+1}=\frac{1}{\Delta t}\left(ik_1\hat{\bar{u}}_{1*}^{n+1}+ik_2\hat{\bar{u}}_{2*}^{n+1}+\frac{\delta}{\delta x_3}\hat{\bar{u}}_{3*}^{n+1}\right) \quad \text{in } \Omega+\partial\Omega, \tag{E 7a}$$

$$\frac{\delta\widehat{\Delta\bar{\Pi}}^{n+1}}{\delta x_3}=\frac{1}{\Delta t}\hat{\bar{u}}_{3*}^{n+1} \quad \text{on } \partial\Omega, \tag{E 7b}$$

$$\hat{\bar{\Pi}}^{n+1}=\hat{\bar{\Pi}}^n+\widehat{\Delta\bar{\Pi}}^{n+1} \quad \text{in } \Omega+\partial\Omega. \tag{E 7c}$$

The velocity at time step $n+1$ becomes

$$\hat{\bar{u}}_1^{n+1}=\hat{\bar{u}}_{1*}^{n+1}-i\;\Delta t\;k_1\widehat{\Delta\bar{\Pi}}^{n+1} \quad \text{in } \Omega+\partial\Omega, \tag{E 8a}$$

$$\hat{\bar{u}}_2^{n+1}=\hat{\bar{u}}_{2*}^{n+1}-i\;\Delta t\;k_2\widehat{\Delta\bar{\Pi}}^{n+1} \quad \text{in } \Omega+\partial\Omega, \tag{E 8b}$$

$$\hat{\bar{u}}_3^{n+1}=\hat{\bar{u}}_{3*}^{n+1}-\Delta t\frac{\delta}{\delta x_3}\widehat{\Delta\bar{\Pi}}^{n+1} \quad \text{in } \Omega+\partial\Omega. \tag{E 8c}$$

At the end of the time step, after the final velocity is computed via (E 8), $\hat{\tilde{u}}_3^{n+1}$ is set to zero on $\partial\Omega$ (the bottom and top boundaries). This is also done for $\hat{\tilde{u}}_1^{n+1}$ and $\hat{\tilde{u}}_2^{n+1}$ on $\partial\Omega_1$ (the bottom boundary).

E.3. *Grid-stretching*

In order to resolve strong gradients in the x_3-direction near the bottom boundary and the top surface, a greater number of points is clustered near these two regions. Consider a set of equidistant points at locations ξ_i discretizing the vertical direction of the domain in figure 1. Clustering or stretching of these points may be accomplished through a mapping hyperbolic function (with existing real inverse) such as

$$z_i = (1/b)\,\tanh[\xi_i\,\tanh^{-1}(b)]. \tag{E 9}$$

This function takes the set of N equidistant points ξ_i discretizing the interval $[-1, 1]$ and maps them to the set of N non-uniformly spaced points z_i in $[-1, 1]$. The points z_i are clustered near the upper and lower bounds of the interval. Coefficient b is a measure of the clustering.

The finite-difference approximations of $\partial/\partial x_3$ and $\partial^2/\partial x_3^2$ used here (i.e. $\delta/\delta x_3$ and $\delta^2/\delta x_3^2$, see Appendix F) can be applied only over points which are equidistant. Thus, derivatives on the non-uniform grid are computed in terms of derivatives on the equidistant grid and derivatives of the inverse of the mapping function as

$$\frac{\mathrm{d}f}{\mathrm{d}z} = \frac{\mathrm{d}f}{\mathrm{d}\xi}\frac{\mathrm{d}\xi}{\mathrm{d}z}, \quad \frac{\mathrm{d}^2 f}{\mathrm{d}z^2} = \frac{\mathrm{d}^2 f}{\mathrm{d}\xi^2}\left(\frac{\mathrm{d}\xi}{\mathrm{d}z}\right)^2 + \frac{\mathrm{d}f}{\mathrm{d}\xi}\frac{\mathrm{d}^2\xi}{\mathrm{d}z^2}, \tag{E 10}$$

where z and ξ denote z_i and ξ_i, respectively, in (E 9). Note that this approach to clustering leads to non-uniformly spaced grid points in the vertical direction only. The grid points are uniformly spaced in the horizontal directions.

E.4. *De-alisasing*

The nonlinear advection term in (E 1) generates scales at high wavenumbers (i.e. small scales) unresolvable by the grid. This effect is reflected through an accumulation of energy at the highest resolvable wavenumbers, often referred to as aliasing. In order to prevent this spurious accumulation, de-aliasing is performed using the well-known 3/2-rule in the horizontal directions. In the vertical direction, the high-order (fourth-order) filter discussed by Slinn & Riley (1998) (see Appendix F) is used in order to attenuate the spurious high-wavenumber energy accumulation while fully preserving the more energetic scales at lower wavenumber. Note that the subgrid-scale closures (the dynamic Smagorinsky and dynamic mixed subgrid-scale stress models) are nonlinear and can give rise to aliasing. However, the contribution of these closures is small and de-aliasing brings about a negligible change in results, thus de-aliasing of the closures was omitted.

E.5. *Validation studies*

Numerous simulations using the previously described method were carried out. The most rigorous were LES and direct numerical simulation (DNS) of turbulent channel flow between parallel walls at $Re = 180$. Looking at results such as mean velocity and resolved Reynolds stresses and one-dimensional spectra, LES performed with the current numerical method was more accurate than LES performed with lower-order discretization methods, as expected. Furthermore, the dynamic Smagorinsky model coefficient in (2.7) was seen to possess the expected asymptotic behaviour in the near-wall region (see Pope 2000). DNS with the current method also performed well

as results on a $(96 \times 96 \times 97)$ grid with $b = 0.923$ were nearly indistinguishable from the DNS results of Kim, Moin & Moser (1997). The DNS of Kim, Moin & Moser was performed on a $(128 \times 128 \times 128)$ grid.

E.6. *Parallel implementation*

The Fortran 90 program executing the numerical method was written in parallel using message passing interface (MPI) protocol. The parallel structure of the code is similar to that presented by Winters, MacKinnon & Mills (2004). When working with variables in real space, the code uses MPI to partition the domain into horizontal (x_1, x_2) slabs on which it can perform horizontal two-dimensional fast Fourier transforms without parallel communications. After the Fourier transforms are performed, the code re-partitions the domain into vertical (x_2, x_3) columns via MPI. Finite-differencing in the x_3-direction is performed on these vertical columns without parallel communications.

Appendix F. Finite-difference stencils

Using compact finite-difference schemes, second- and first-order derivatives of function $f(z)$ on $[a, b]$ are obtained. Consider the set $\{z_1, z_2, z_3, \cdot s, z_N, z_{N+1}\}$ of equidistant points gridding the interval $[a, b]$ with h being the distance between the points. The second and first derivatives of $f(z)$ may be obtained from

$$\boldsymbol{A}\boldsymbol{f}'' = \boldsymbol{B}\boldsymbol{f} \quad \text{thus} \quad \boldsymbol{f}'' = \{\boldsymbol{A}^{-1}\boldsymbol{B}\}\boldsymbol{f} \tag{F 1}$$

and

$$\boldsymbol{C}\boldsymbol{f}' = \boldsymbol{D}\boldsymbol{f} \quad \text{thus} \quad \boldsymbol{f}' = \{\boldsymbol{C}^{-1}\boldsymbol{D}\}\boldsymbol{f} \tag{F 2}$$

where $\boldsymbol{f} = (f_1, f_2, \cdot s, f_N)^t$ and f_i is $f(z)$ evaluated at $z_i \in [a, b]$. Matrices $\boldsymbol{A}$, $\boldsymbol{B}$, $\boldsymbol{C}$ and $\boldsymbol{D}$ are banded. However, matrices $\boldsymbol{A}^{-1}\boldsymbol{B}$ and $\boldsymbol{C}^{-1}\boldsymbol{D}$ are full. Next, the stencils used to generate these matrices are detailed.

F.1. *First-order derivative*

Let f_i' denote the first derivative of $f(z)$ at $z = z_i$. For $i > 2$ and $i < N$, the first derivative of function $f(z)$ is approximated via

$$\tfrac{1}{3} f'_{i-1} + f'_i + \tfrac{1}{3} f'_{i+1} = \tfrac{1}{h}\left(-\tfrac{1}{36} f_{i-2} - \tfrac{7}{9} f_{i-1} + \tfrac{7}{9} f_{i+1} + \tfrac{1}{36} f_{i+2}\right). \tag{F 3}$$

Detailed analysis of this $O(h^6)$ approximation is given by Lele (1992). For $i = 1$, the first derivative may be obtained from the following $O(h^5)$ approximation:

$$f'_1 = \frac{1}{h}\left(c_1 f_1 + c_2 f_2 + c_3 f_3 + c_4 f_4 + c_5 f_5 + c_6 f_6 + c_7 f_7 + c_8 f_8\right) \tag{F 4}$$

where

$$c_1 = -(\alpha_0 - 28\beta_0 + 13068)/5040, \tag{F 5a}$$

$$c_2 = +(\alpha_0 - 27\beta_0 + 5040)/720, \tag{F 5b}$$

$$c_3 = -(\alpha_0 - 26\beta_0 + 2520)/240, \tag{F 5c}$$

$$c_4 = +(\alpha_0 - 25\beta_0 + 1680)/144, \tag{F 5d}$$

$$c_5 = -(\alpha_0 - 24\beta_0 + 1260)/144, \tag{F 5e}$$

$$c_6 = +(\alpha_0 - 23\beta_0 + 1008)/240, \tag{F 5f}$$

$$c_7 = -(\alpha_0 - 22\beta_0 + 840)/720, \tag{F 5g}$$

$$c_8 = +(\alpha_0 - 21\beta_0 + 720)/5040, \tag{F 5h}$$

$\alpha_0 = 1809.257$ and $\beta_0 = -65.1944$. For $i = 2$, the first derivative may be obtained from the following $O(h^5)$ approximation:

$$f_2' = \frac{1}{h}\left(d_1 f_1 + d_2 f_2 + d_3 f_3 + d_4 f_4 + d_5 f_5 + d_6 f_6 + d_7 f_7 + d_8 f_8\right) \tag{F 6}$$

where

$$d_1 = -(\alpha_1 - 21\beta_1 + 720)/5040, \tag{F 7a}$$

$$d_2 = +(\alpha_1 - 20\beta_1 - 1044)/720, \tag{F 7b}$$

$$d_3 = -(\alpha_1 - 19\beta_1 - 720)/240, \tag{F 7c}$$

$$d_4 = +(\alpha_1 - 18\beta_1 - 360)/144, \tag{F 7d}$$

$$d_5 = -(\alpha_1 - 17\beta_1 - 240)/144, \tag{F 7e}$$

$$d_6 = +(\alpha_1 - 16\beta_1 - 180)/240, \tag{F 7f}$$

$$d_7 = -(\alpha_1 - 15\beta_1 - 144)/720, \tag{F 7g}$$

$$d_8 = +(\alpha_1 - 14\beta_1 - 120)/5040, \tag{F 7h}$$

$\alpha_1 = -262.16$ and $\beta_1 = -26.6742$. Similar expressions for the first derivatives are defined at $i = N$ and $i = N + 1$. The stencils in (F 4)–(F 7*h*) are analysed in detail by Carpenter, Gottlieb & Abarbanel (1993).

F.2. *Second-order derivative*

For $i > 2$ and $i < N$, the second derivative of function $f(z)$ is computed using the following $O(h^6)$ approximation discussed by Lele (1992):

$$\tfrac{2}{11} f_{i-1}' + f_i' + \tfrac{2}{11} f_{i+1}' = \tfrac{1}{h^2}\left(\tfrac{3}{44} f_{i-2} + \tfrac{12}{11} f_{i-1} - \tfrac{51}{22} f_i + \tfrac{12}{11} f_{i+1} + \tfrac{3}{44} f_{i+2}\right). \tag{F 8}$$

For $i = 1$, the second derivative may be obtained from the following $O(h^5)$ approximation:

$$f_1'' = \frac{1}{h^2}\left(c_1 f_1 + c_2 f_2 + c_3 f_3 + c_4 f_4 + c_5 f_5 + c_6 f_6 + c_7 f_7 + c_8 f_8\right), \tag{F 9}$$

where $c_1 = 5.211$, $c_2 = -22.300$, $c_3 = 43.950$, $c_4 = -52.722$, $c_5 = 41.000$, $c_6 = -20.100$, $c_7 = 5.661$ and $c_8 = -0.700$. For $i = 2$, the second derivative may be obtained from the following $O(h^5)$ approximation:

$$f_2'' = \frac{1}{h^2}\left(d_1 f_1 + d_2 f_2 + d_3 f_3 + d_4 f_4 + d_5 f_5 + d_6 f_6 + d_7 f_7 + d_8 f_8\right), \tag{F 10}$$

where $d_1 = 0.700$, $d_2 = -0.389$, $d_3 = -2.700$, $d_4 = 4.750$, $d_5 = -3.722$, $d_6 = 1.800$, $d_7 = -0.500$ and $d_8 = 0.061$. Similar expressions for the second derivatives are defined at $i = N$ and $i = N + 1$. The stencils in (F 9) and (F 10) are courtesy of T. L. Jackson (University of Illinois at Urbana-Champaign, personal communication) and may be derived using a similar approach to that of Carpenter *et al.* (1993).

When solving the Poisson's equation for pressure in (E 7*c*), the following alternative expressions are used (instead of (F 9)–(F 10)) leading to lower round-off errors. For $i = 1$,

$$f_1'' = -\frac{1}{h}\frac{49}{10} f_1' + \frac{1}{h^2}\left(\frac{13\,489}{1800} f_1 + 12 f_2 - \frac{15}{2} f_3 + \frac{40}{9} f_4 - \frac{15}{8} f_5 + \frac{12}{25} f_6 - \frac{1}{18} f_7\right) \tag{F 11}$$

with truncation error $0.6572h^6 \mathrm{d}^8 f/\mathrm{d}z^8$. Note that the Neumann pressure boundary condition in (E 7*c*) is assigned through the first term in the right-hand side of (F 11). For $i = 2$,

$$\frac{11}{128} f''_{i-1} + f''_i + \frac{11}{128} f''_{i+1} = \frac{1}{h^2}\left(\frac{585}{512} f_1 - \frac{141}{64} f_2 + \frac{459}{512} f_3 + \frac{9}{32} f_4 - \frac{85}{512} f_5 + \frac{3}{64} f_6 - \frac{3}{512} f_7\right) \quad \text{(F 12)}$$

with truncation error $0.02101h^6 d^8 f/dz^8$. Similar expressions are used for $i = N+1$ and $i = N$. The approximations in (F 11) and (F 12) and their corresponding truncation errors were derived via Taylor series analysis.

F.3. *Spatial filtering of advection terms*

As discussed earlier, the advection terms in the momentum equations are spatially filtered in the vertical direction in order to damp out scales of motion unresolvable by the grid. The following fourth-order compact filter adapted for a non-uniform grid (Slinn & Riley 1998) is used:

$$\begin{aligned} 0.4\tilde{f}_{i-1} + \tilde{f}_i + 0.4\tilde{f}_{i+1} = {} & 0.4 f_{i-1} + f_i + 0.4 f_{i+1} \\ & - \frac{1}{80}(f_{i+2} - 4f_{i+1} + 6f_i - 4f_{i-1} + f_{i-2}) \\ & - \frac{h}{80}\left(\frac{6\gamma_2(z_i)}{\gamma_1^2(z_i)}\right)\left(\frac{f_{i+2} - 2f_{i+1} + 2f_{i-1} - f_{i-2}}{2}\right) \\ & - \frac{h^2}{80}\left(\frac{4\gamma_3(z_i)}{\gamma_1^3(z_i)} + \frac{3\gamma_2^2(z_i)}{\gamma_1^4(z_i)}\right)(f_{i+1} - 2f_i + u_{i-1}) \\ & - \frac{h^3}{80}\left(\frac{\gamma_4(z_i)}{\gamma_1^4(z_i)}\right)\left(\frac{f_{i+1} - f_{i-1}}{2}\right) \end{aligned} \quad \text{(F 13)}$$

where $\gamma_1 = \partial\xi/\partial z$, $\gamma_2 = \partial^2\xi/\partial z^2$, $\gamma_3 = \partial^3\xi/\partial z^3$, $\gamma_4 = \partial^4\xi/\partial z^4$ and ξ is the mapping function in (E 9). Note that this stencil is not valid for points at the bottom and top boundaries and for the first two horizontal planes of points off these boundaries. In the current implementation, the filter is not applied at these points. This omission does not have a negative impact on results.

A formal derivation of this compact filter can be made through Taylor series analysis. From this analysis, we can see that the filtered function is an approximation of the unfiltered function up to fourth-order. That is

$$\tilde{f} = f + O(h^4). \quad \text{(F 14)}$$

The finite-difference approximations of the first and second derivatives in the vertical (x_3) direction (discussed in the previous subsection) introduce an error of $O(h^5)$ or higher. Filtering the advection terms in the vertical direction using (F 13) introduces an error of $O(h^4)$. Furthermore, using a spectral discretization in the horizontal (x_1 and x_2) directions introduces an error of much higher order than the previously discussed finite differencing and filtering operations. Thus, the current spatial discretization is at least $O(h^4)$. A higher-order filter could potentially be introduced; however, this would involve a more expensive computation at the expense of only minimally changing results.

REFERENCES

Armfield, S. W. & Street, R. 2000 Fractional step methods for the Navier–Stokes equations on non-staggered grids. *ANZIAM J.* **42(E)**, C134–C156.

Andrews, D. G. & McIntyre, M. E. 1978*a* An exact theory of nonlinear waves on Lagrangian-mean flow. *J. Fluid Mech.* **89**, 609–646.

Andrews, D. G. & McIntyre, M. E. 1978*b* On wave-action and its relatives. *J. Fluid. Mech.* **89**, 647–664 (and corrigendum **95**, 796).

Bech, K. H., Tillmark, N., Alfredsson, H. & Andersson, H. I. 1995 An investigation of turbulent plane Couette flow at low Reynolds numbers. *J. Fluid Mech.* **73**, 401–426.

Carpenter, M. H., Gottlieb, D. & Abarbanel, S. 1993 The stability of numerical boundary treatments for compact high-order finite-difference schemes. *J. Comput. Phys.* **108**, 272–292.

Chini, G. P. & Leibovich, S. 2003 Resonant Langmuir-circulation–internal-wave interaction. Part 1. Internal wave reflection. *J. Fluid Mech.* **495**, 33–55.

Chini, G. P. & Leibovich, S. 2005 Resonant Langmuir-circulation–internal-wave interaction. Part 2. Langmuir circulation instability. *J. Fluid Mech.* **524**, 99–120.

Craik, A. D. D. 1977 The generation of Langmuir circulations by an instability mechanism. *J. Fluid Mech.* **81**, 209–223.

Craik, A. D. D. 1985 *Wave Interactions and Fluid Flows.* Cambridge University Press.

Craik, A. D. D. & Leibovich, S. 1976 A rational model for Langmuir circulation. *J. Fluid Mech.* **73**, 401–426.

Cox, S. M. & Leibovich, S. 1993 Langmuir circulations in a surface layer bounded by a strong thermocline. *J. Phys. Oceanogr.* **23**, 1330–1345.

Cox, S. M. & Leibovich, S. 1994 Large-scale Langmuir circulation and double-diffusive convection: evolution equations and flow transitions. *J. Fluid Mech.* **276**, 189–210.

Cox, S. M. & Leibovich, S. 1997 Large-scale three-dimensional Langmuir circulation. *Phys. Fluids* **9**, 2851–2863.

Gargett, A. E. & Wells, J. R. 2007 Langmuir turbulence in shallow water. Part 1. Observations. *J. Fluid Mech.* **576**, 27–61.

Gargett, A., Wells, R., Tejada-Martínez, A. E. & Grosch, C. E. 2004 Langmuir supercells: a dominant mechanism for sediment resuspension and transport. *Science* **306**, 1925–1928.

Holm, D. D. 1996 The ideal Craik–Leibovich equations. *Physica* D **98**, 415–441.

Kim, J., Moin, P. & Moser, R. 1987 Turbulence statistics in fully developed channel flow at low Reynolds number. *J. Fluid Mech.* **177**, 133–166.

Langmuir, I. 1938 Surface motion induced by the wind. *Science* **87**, 119–123.

LeBlond, P. H. and Mysak, L. A. 1978 *Waves in the Ocean.* Elsevier.

Lee, M. J. & Kim, J. 1991 The structure of turbulence in a simulated plane Couette flow. In *Proc. 8th Symp. Shear Flows, Munich, Germany*, paper 5-3.

Leibovich, S. 1977*a* On the evolution of the system of wind drift currents and Langmuir circulations in the ocean. Part 1. Theory and averaged current. *J. Fluid Mech.* **79**, 715–743.

Leibovich, S. 1977*b* Convective instability of stably stratified water in the ocean. *J. Fluid Mech.* **82**, 541–581.

Leibovich, S. 1980 On wave–current interaction theories of Langmuir circulations. *J. Fluid Mech.* **99**, 715–724.

Leibovich, S. 1983 The form and dynamics of Langmuir circulations. *Annu. Rev. Fluid Mech.* **15**, 391–427.

Leibovich, S. 1985 Oscillatory and competing instabilities in a nonlinear model for Langmuir circulations. *Phys. Fluids* **28**, 2050–2061.

Leibovich, S. & Radhakrishnan, K. 1977 On the evolution of the system of wind drift currents and Langmuir circulations in the ocean. Part 2. Structure of the Langmuir vortices. *J. Fluid Mech.* **80**, 481–507.

Leibovich, S. & Tandon, A. 1993 Three dimensional Langmuir circulations and stability in a stratified layer. *J. Geophys. Res.* **98**, 16 501–16 508.

Leibovich, S., Lele, S. K. & Moroz, I. 1989 Nonlinear dynamics in Langmuir circulations and in thermosolutal convection. *J. Fluid Mech.* **198**, 471–511.

Lele, S. K. 1992 Compact finite difference schemes. *J. Comput. Phys.* **103**, 16–42.

Li, M., Garrett, C. & Skyllingstad, E. 2005 A regime diagram for classifying turbulent large eddies in the upper ocean. *Deep-Sea Res.* I **52**, 259–278.

Lilly, D. K. 1992 A proposed modification of the Germano subgrid-scale closure. *Phys. Fluids* **3**, 2746–2757.

Lumley, J. L. 1978 Computational modeling of turbulent flows. In *Adv. Appl. Mech.* **18**, 123–176.

Lund, T. S. 1997 On the use of discrete filters for large-eddy simulation. In *Annu. Res. Briefs*, Center for Turbulence Research, NASA Ames/Stanford University, pp. 83–95.

McWilliams, J. C., Sullivan, P. P. & Moeng, C.-H. 1997 Langmuir turbulence in the ocean. *J. Fluid Mech.* **334**, 1–30.

Moser, R., Kim, J. & Mansour, N. M. 1999 Direct numerical simulation of turbulent channel flow up to $Re_\tau = 590$. *Phys. Fluids* **11**, 943–945.

Morinishi, Y. & Vasilyev, O. V. 2001 A recommended modification to the dynamic two-parameter mixed subgrid scale model for large eddy simulation of turbulent flows. *Phys. Fluids* **13**, 3400–3410.

Noh, Y., Min, H.-S. & Raasch, S. 2004 Large eddy simulation of the ocean mixed layer: the effects of wave breaking and Langmuir circulation. *J. Phys. Oceanogr.* **34**, 720–735.

Papavassiliou, D. V. & Hanratty, T. J. 1997 Interpretation of large-scale structures observed in a turbulent plane Couette flow. *Intl J. Heat Fluid Flow* **18**, 55–69.

Phillips, O. M. 1967 *Dynamics of the Upper Ocean.* Cambridge University Press.

Pope, S. B. 2000 *Turbulent Flows.* Cambridge University Press.

Skyllingstad, E. D. & Denbo, D. W. 1995 An ocean large eddy simulation of Langmuir circulations and convection in the surface mixed layer. *J. Geophys. Res.* **100**, 8501–8522.

Skyllingstad, E. D., Smyth, W. D., Moum, J. N. & Wijesekera, H. 1999 Upper-ocean turbulence during a westerly wind burst: a comparison of large-eddy simulation results and microstructure measurements. *J. Phys. Oceanogr.* **29**, 5–28.

Slinn, D. N. & Riley, J. J. 1998 A model for the simulation of turbulent boundary layers in an incompressible stratified flow. *J. Comput. Phys.* **144**, 550–602.

Smagorinsky, J. 1963 General circulation experiments with the primitive equations. I. The basic experiment. *Mon. Weather Rev.* **91**, 99–164.

Sullivan, P. P., McWilliams, J. C. & Melville, W. K. 2005 Surface waves and oceanic mixing: insights from numerical simulations with stochastic surface forcing. In *Proc. of the 14th 'Aha Huliko'a Hawaiian Winter Workshop*, pp. 147–155.

Tandon, A. & Leibovich, S. 1995*a* Secondary instabilities in Langmuir circulations *J. Phys. Oceanogr.* **25**, 1206–1217.

Tandon, A. & Leibovich, S. 1995*b* Simulations of three-dimensional Langmuir circulation in water of constant density. *J. Geophys. Res.* **100**, 22 613–22 623.

Thorpe S. 2004 Langmuir Circulation. *Annu. Rev. Fluid Mech.* **36**, 55–79.

Tsukahara, T. & Kawamura, H. 2004 Large scale structure captured in DNS of turbulent Couette and Poiseuille flows. *Second Intl Workshop on Wall-Bounded Turbulent Flows, Trieste, Italy.*

Winters, K. B., MacKinnon, J. A. & Mills, B. 2004 A spectral model for process studies of rotating density-stratified flows. *J. Atmos. Ocean. Technol.* **21**, 69–94.